ELSEVIER

Available online at www.sciencedirect.com

ScienceDirect

C. R. Physique 10 (2009) 352–378

Comptes Rendus Physique

Metamaterials / Métamatériaux

Negative refractive index, perfect lenses and checkerboards: Trapping and imaging effects in folded optical spaces

Sébastien Guenneau [a,*], S. Anantha Ramakrishna [b,c]

[a] *Department of Mathematical Sciences, University of Liverpool, Liverpool L69 3BX, United Kingdom*
[b] *Department of Physics, Indian Institute of Technology, Kanpur 208016, India*
[c] *Indian Institute of Science Education and Research, Mohali, Transit Campus, MGSIPA Complex, Sector 26, Chandigarh 160019, India*

Abstract

Newly discovered metamaterials have opened new vistas for better control of light via negative refraction, whereby light refracts in the “wrong” manner. These are dielectric and metallic composite materials structured at subwavelength lengthscales. Their building blocks consist of local resonators such as conducting thin bars and split rings driving the material parameters such as the dielectric permittivity and magnetic permeability to negative (complex) values. Combined together, these structural elements can bring about a (complex valued) negative effective refractive index for the Snell–Descartes law and result in negative refraction of radiation. Negative refractive index materials can support a host of surface plasmon states for both polarizations of light. This makes possible unique effects such as imaging with subwavelength image resolution through the Pendry–Veselago slab lens. Other geometries have also been investigated, such as cylindrical or spherical lenses that enable a magnification of images with subwavelength resolution. Superlenses of three-fold (equilateral triangle), four-fold (square) and six-fold (hexagonal) geometry allow for multiple images, respectively two, three, and five. Generalization to rectangular and triangular checkerboards consisting of alternating cells of positive and negative refractive index represents a very singular situation in which the density of modes diverges at the corners, with an infinity of images. Sine-cosecant anisotropic heterogeneous square and triangular checkerboards can be respectively mapped onto three-dimensional cubic and icosahedral corner lenses consisting of alternating positive and negative refractive regions. All such systems with corners between negative and positive refractive media display very singular behavior with the local density of states becoming infinitely large at the corner, in the limit of no dissipation. We investigate all of these, using the unifying viewpoint of transformation optics. ***To cite this article: S. Guenneau, S.A. Ramakrishna, C. R. Physique 10 (2009).***

Résumé

Réfraction négative, lentilles parfaites et échiquiers : piégeage et imagerie dans des espaces optiques repliés. Les métamatériaux, structures diélectriques et métalliques dont la périodicité est inférieure à la longueur d’onde, ouvrent de nouveaux horizons dans le contrôle de la lumière par le truchement de la réfraction négative, où la lumière prend un mauvais tour. Leur brique élementaire est constitutée d’une part d’un résonateur de type anneau fendu qui conduit la perméabilité à prendre des valeurs négatives, et d’autre part d’une barre métallique qui joue un rôle similaire pour la permittivité. A l’échelle macroscopique, ils prennent la forme de lentilles plates, cylindriques et sphériques (dont celle éponyme imaginée par Victor Veselago en 1968 et dont John Pendry dé-

---

[*] Corresponding author.
E-mail addresses: guenneau@liverpool.ac.uk (S. Guenneau), sar@iitk.ac.in (S.A. Ramakrishna).

1631-0705/$ – see front matter © 2009 Published by Elsevier Masson SAS on behalf of Académie des sciences.
doi:10.1016/j.crhy.2009.04.002

montre qu'elle est parfaite en l'an 2000), ou d'échiquiers et de solides platoniques qui piègent la lumière en leur sein. ***Pour citer cet article : S. Guenneau, S.A. Ramakrishna, C. R. Physique 10 (2009).***

Keywords: Surface modes; Negative refraction; Lenses; Resonators; Geometric transforms

Mots-clés : Modes de surface ; Réfraction négative ; Lentilles ; Résonateurs ; Transformations géométriques

Version française abrégée

Cet article présente une revue des lentilles dites de Pendry–Veselago [1,2], qui repoussent les limites de l'optique classique (de Fourier) en s'affranchissant du critère de Rayleigh. Ce pendant de l'inégalité d'Heisenberg en mécanique quantique postule que la résolution d'une image par un système optique traditionnel ne peut-être inférieure à la moitié de la longueur d'onde émise par la source.

Nous commençons par un rappel historique dans l'introduction (Section 1) des différentes étapes qui ont mené à la découverte des lentilles parfaites, en rendant justice à l'article visionnaire de McPhedran, Nicorovici et Milton [3] sur une lentille cylindrique parfaite, dont la publication précoce (en 1994, l'avénement des métamatériaux n'avait pas encore eu lieu) semble avoir joué en sa défaveur (l'histoire de la physique se nourrit de paradoxes). Nous expliquons comment cette cure de jouvence de l'optique classique a été rendue possible grâce aux matériaux d'indice négatif, qui ont été découverts par Sir John Pendry et ses collaborateurs entre 1996 (introduction d'un réseau de fils métalliques fins) et 1999 (introduction d'un réseau de doubles anneaux fendus). En bref, ces deux ingrédients, quant ils sont combinés, conduisent à des matériaux caractérisés par un indice de réfraction négatif dans les lois de Snell–Descartes. De tels métamatériaux sont aujourd'hui connus pour leurs propriétés plasmoniques agissant à la fois sur les composantes électrique et magnétique du champ. Ces vertues rendent possible des phénomènes uniques tels qu'une image sans aberation ni astigmatisme (Veselago, 1968 [2]), qui présente de surcroît une résolution sous-longueur d'onde (Pendry, 2000 [1]), à travers leur lentille plate éponyme.

Nous passons ensuite en revue les propriétés mathématiques des matériaux main-gauche (raisons motivant le choix d'une racine carrée négative dans le plan complexe en Section 2) et la physique sous-jacente (homogénéisation de structures périodiques localement résonantes en Section 3). Nous expliquons en détails pourquoi la pierre de touche de ces métamatériaux réside dans un modèle de Drude qui rend compte du comportement effectif du réseau d'anneaux fendus et de fils métalliques qui les compose, ce que John Pendry avait démontré en faisant appel à son intuition physique dès la fin du siècle dernier (des mathématiciens appliqués ont depuis lors fournit un cadre théorique adéquat). Plus précisément, lorsque les anneaux sont traversés par une onde électromagnétique, les électrons tournent d'une extrémité à l'autre dans les deux sens, de sorte que les boucles se comportent comme des solénoïdes induisant du magnétisme artificiel : le métamatériau posséde alors une perméabilité négative. Par ailleurs, chaque segment de fil métallique se comporte comme un dipôle électrique et les électrons vont et viennent tout du long. Ce type de résonance dite plasmonique s'observe dans les métaux, dont certains comme l'or ou l'argent possèdent une permittivité négative dans le spectre visible. L'apport de John Pendry en 1996 a été de diluer le métal dans du diélectrique pour rendre le matériau suffisamment transparent (one notera que les métaux sont fortement absorbant dans le visible). Pour des raisons de causalité, une permittivité et une perméabilité négatives aux mêmes fréquences conduisent à un indice de réfraction négatif. Cette coïncidence ne se produit pas dans les matériaux à l'état naturel, mais elle a été observée expérimentalement pour des métamatériaux fonctionnant du domaine micro-ondes au proche infra-rouge.

Nous suivons ensuite Alice, l'égérie de Lewis Carroll, de l'autre côté du miroir dans les sections suivantes. Nous adoptons tout d'abord un point de vue géométrique en Section 4 qui lève un coin du voile sur la physique de la réfraction négative : pour fabriquer des lentilles parfaites ad libitum, on procède à un repliement de l'espace optique sur lui-même (pour obtenir une image clône de la source – ou image parfaite – il suffit d'annuler le chemin optique). Or, pour paraphraser l'énoncé du principe de Pierre Fermat, la lumière suit toujours le trajet le plus court. Pour annuler son chemin optique, il suffit donc de replier l'espace sur lui-même, ce qui revient à introduire une métrique négative dans les équations de Maxwell. Dans une lentille classique, le chemin optique ne s'annule pas et l'image d'un point n'est généralement pas un point, mais une tache ou astigmatisme (mis à part peut-être des techniques de microscopie confocales en champ proche ou des reconstructions d'image utilisant des algorithmes pour problèmes inverses qui nécessitent un outil informatique). L'idée est donc de réduire le chemin optique. Par ailleurs, les aberrations qui affectent la qualité des images, peuvent-être minimisées. La lentille plate de Pendry–Veselago fait très bien ce travail, avec une source et une image situées à une distance finie de la lentille.

Mais d'autres géométries ont été envisagées, telles que des lentilles cylindriques ou sphériques qui permettent un grossissement d'une image parfaite [4]. Et il y a plus, des lentilles triangulaire, carrée et hexagonale permettent d'obtenir respectivement deux, trois et cinq images parfaites. Leur généralisation à des échiquiers triangulaire et rectangulaire [5] dont les cases alternent des matériaux d'indice de réfraction positif et négatif représente une situation pour le moins singulière dans laquelle la densité de mode à chaque coin diverge, avec en prime une infinité d'images. Pour peu qu'ils présentent un certain type d'hétérogénéité et d'anisotropie que nous qualifions de sinus-cosinus, ces échiquiers peuvent-être envoyés sur des lentilles parfaites cubiques et icosahédrales constituées respectivement de huit et vingt régions infinies alternant des matériaux homogènes isotropes d'indices de réfraction positif et négatif. Ces coins parfaits tri-dimensionnels présentent une densité locale d'état infinie au noeud central, pourvu que la dissipation inhérente dans ces métamatériaux tende vers zéro. Dans cet article de revue, nous abordons toutes ces lentilles à travers le point de vue unificateur de l'optique de transformation.

Dans les Sections 5 et 6, nous explorons ces différentes classes de lentilles parfaites, avec en point de mire les échiquiers d'Alice, qui permettent de piéger la lumière. Ces résonateurs d'un genre nouveau supportent des modes de plasmon infiniment dégénérés quand ils pavent l'espace tout entier, et donc ils exhibent une densité d'état locale qui n'est limitée que par la taille de ces échiquiers (et leur dissipation). Quand ils sont finis suivant une direction d'espace, ces échiquiers offrent un paradigme optique : un tracé de rayons suggère qu'ils réfléchissent tout ou partie de la lumière, alors qu'elle est intégralement transmise (transmission extraordinaire).

Nous concluons cet article de revue en Section 7 avec les perspectives offertes par la réfraction négative et d'autres voies de recherche prometteuses telles que l'ultra-réfraction étudiée par Stefan Enoch et ses collaborateurs [6]. Dans ce cas de figure, l'indice de réfraction est proche de zéro, et les relations de Snell–Descartes nous apprennent alors que tout rayon incident sur un tel slab sera transmis suivant une direction perpendiculaire à l'interface air-slab. On peut dès lors envisager des antennes omni-directionnelles. Enfin, Graeme Milton et Nicolae Nicorovici ont ouvert une voie originale en démontrant mathématiquement et numériquement qu'une lentille parfaite cylindrique permet de rendre invisible un ensemble de dipôles placés dans son voisinage immédiat [7] (cloaking).

1. Introduction

A fundamental issue with imaging systems is the constraint on resolution imposed by the diffraction limit. In ordinary imaging systems that image only the propagating modes of radiation, features on the object smaller than the wavelength cannot be reproduced in the image. Images with sub-wavelength features can be assembled from scanning probes that can sense the electromagnetic near-fields (popularly known as scanning near-field optical microscopy). However, the scanning process severely limits image frame rates, and the probes require near direct contact with the object. The perfect lens proposed by Sir John Pendry in 2000 began to address these issues by providing for the possibility of image transfer of both the near- and far-field components of radiation with a free-space working distance [1]. The cornerstone of this flat lens is the concept of negative refraction – foreseen by Victor Veselago in the late 1960s [2] – whereby both permittivity and permeability take negative values and lead to negative refractive index and near-field enhancements. The subwavelength details of the source are transmitted through the system because they couple to the surface plasmons that exist on the boundaries between the negative refractive index material and the dielectric medium. This plasmonic mechanism is also the basis for the current interest in metallic structures for super-resolution imaging at optical frequencies. Although such a near-field magnifier for electrostatic fields in the cylindrical geometry was proposed earlier by McPhedran, Nicorovici and Milton [3], these perfect lenses can be flat and can be generalized to a variety of geometries including the cylindrical and spherical geometries [8]. There are some fundamental differences in the different geometries, for example, the focal surfaces. The cylindrical lens has curved object and image surfaces, whereas the perfect lens has planar object and image planes that better match typical detector arrays, and display formats. These imaging devices enabled by negative refractive index metamaterials have attracted a lot of attention and activity during the past few years [9].

It was subsequently realized that the image resolution of these devices made of negative refractive index materials suffered from serious limitations due to the presence of dissipation and spatial dispersion [10] that is inherent to the structured composite resonant metamaterials. Pendry had proposed [1] that a thin film of silver that has negative dielectric permittivity alone can approximately act as a superlens with subwavelength image resolution at visible and near ultra-violet frequencies for p-polarized light. Refinements of the Pendry lens were subsequently considered to improve the performance using the metamaterials at hand: the superlens effect was generalized to an asymmetric system, for example, a silver film with glass on one side and air on the other which made the system mechanically more robust. Further, the image resolution obtained by an asymmetric lens could be better under certain conditions. This proposal by Pendry and Ramakrishna to use a film of silver, which displays a (complex valued) negative dielectric constant in the visible spectrum, with air on one side and other media such as glass or GaAs on the other side [11] led to the demonstration of subwavelength imaging through negative refraction by Zhang's team [12]. Such an asymmetric lossy near-perfect lens for p-polarized waves can be further improved. Implementation strategies for near-field magnification have been explored with layered media [13–15]. Such devices are sometimes called hyper-lenses, so named because they are composed of an indefinite medium [16] with a hyperbolic dispersion relation. Experimental realizations have also appeared using layered media [17,18], and wire arrays [19]. For a fixed input aperture, the near-field magnification actually increases the amount of image information available in the far field. If one has both a free-space working distance and near-field magnification one can acquire high resolution, sub-diffraction images using standard resolution detectors, and without being in actual physical contact with the object.

In this review, we present the theory of negative refractive index materials that can operate as superlenses with subwavelength image resolution. We first look at two ways of producing a metamaterial with the desired properties: either by making a system of thin, alternating metal and dielectric layers which is an indefinite metamaterial, or with an array of split ring resonators and conducting thin wires. A system of the former type was proposed by Ramakrishna et al. [13] as a form of superlens, and it improves the original suggestion for a superlens [1], which consists of just a single layer of metal (as realized by the team of Zhang [12]). We then look at the dispersion relation for our anisotropic material, to see why modes which would be evanescent in both the metal and the dielectric separately are able to propagate in the combined system, and why there is a preferred direction of propagation. The latter type of metamaterial, first introduced by Pendry and co-workers in 1999 [20], is based upon the existence of a low-frequency stop band associated with the local resonance of the periodically arranged split ring resonators [21]. Next, we investigate the transmission properties of a slab of negative refractive index material, and explain the superlens imaging processes. Then we move on to the generalization of the Pendry–Veselago lens to *optical complementary media* whereby the combined effect on light propagating through two regions of space, with spatially varying properties and related in a prescribed manner, get nullified. Using this generalization and a powerful technique of geometric transformations, we show how to design varied generalized lenses that provide for a variety of useful functions: including magnification and light confinement, that operate on both the near- and far-field, and can also provide for free-space working distances.

2. Through the looking glass: A positively negative square root

Let us understand why should a medium with $\Re e(\epsilon) < 0$ and $\Re e(\mu) < 0$ be considered to have a negative refractive index. There is a subtlety with the definition of the refractive index through the Maxwell relation $n = \sqrt{\varepsilon\mu}$ in the negative layer. Care has to be taken for the choice of the square root in the definition of n. Indeed, the constitutive parameters for a medium with both $\Re e(\epsilon) < 0$ and $\Re e(\mu) < 0$ satisfy

$$\varepsilon = |\varepsilon| e^{i\Phi_\varepsilon}, \quad \mu = |\mu| e^{i\Phi_\mu}, \quad \text{where } \Phi_\varepsilon, \Phi_\mu \in \left[\frac{\pi}{2}, \pi\right] \tag{1}$$

This leads to an ambiguity in the expression for the refractive index n:

$$n = |n| e^{i\Phi_n}, \quad \text{with } \Phi_n = \frac{1}{2}(\Phi_\mu + \Phi_\varepsilon) \in \left[\frac{\pi}{2}, \pi\right] \quad \text{or} \quad \Phi_n = \frac{1}{2}(\Phi_\mu + \Phi_\varepsilon) - \pi \in \left]-\frac{\pi}{2}, 0\right] \tag{2}$$

depending upon the choice for the square root. We infer from (2) that the wave is either left-handed with respect to the wave vector **k** and right-handed with respect to the direction of the energy flow given by the Poynting vector **S** ($\Re e(n) < 0$ and $\Im m(n) > 0$) or right-handed with respect to **k** and **S** ($\Re e(n) > 0$ and $\Im m(n) < 0$). Either physical situation seems acceptable.

As we are particularly interested in the case of small loss, we can take the following two ansatz:

$$\varepsilon = \varepsilon_r + i\eta\varepsilon_i \quad \text{and} \quad \mu = \mu_r + i\eta\mu_i \quad \text{where } 0 < \eta \ll 1 \tag{3}$$

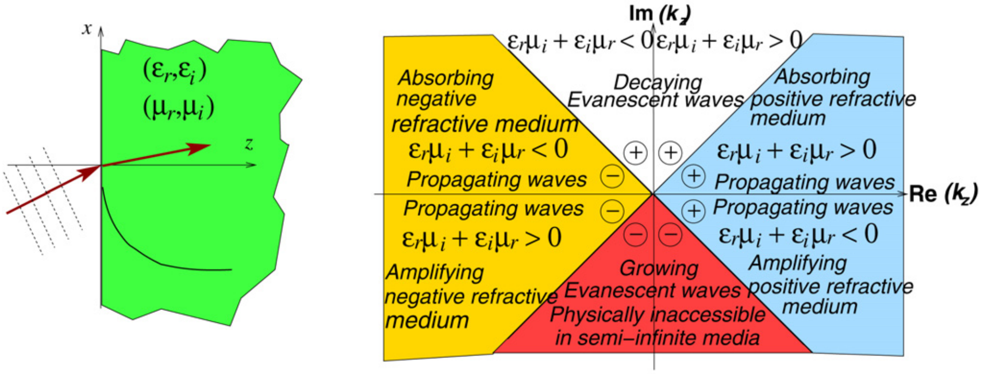

Fig. 1. A scheme for the classification of electromagnetic media into combinations of positive refractive or negative refractive media (sign of the real part of the wave-vector given in the various regions) and absorbing or amplifying media.

where ε_r and μ_r are negative reals, whereas ε_i and μ_i are positive reals. We obtain

$$n = \pm\sqrt{|\varepsilon_r \mu_r|}\left[1 - i\frac{\eta}{2}\left(\frac{\varepsilon_i}{|\varepsilon_r|} + \frac{\mu_i}{|\mu_r|}\right)\right] + O\left(\eta^2\right) \tag{4}$$

We note that a refractive index n such that $\Re e(n) > 0$ and $\Im m(n) < 0$ corresponds to an exponentially growing wave in a dissipative medium and should therefore be disregarded in (4). Taking the limit of zero absorption (η goes to zero) in (4) for $\Re e(n) < 0$ and $\Im m(n) > 0$, gives $n = -\sqrt{|\varepsilon_r \mu_r|}$. This is a standard practice in Physics to obtain the causal solution by considering a lossy medium and taking the limit of zero loss.

For simplicity, we only considered the case of passive media, but the general issue of resolving the wave vector in negative refractive media with gain can be also addressed. For this, one has to consider the analytic behavior of the wave vector **k** in the complex plane, with a total of eight physically distinct cases in the four quadrants of two Riemann sheets [22]. The eight cases along with the different media and circumstances are shown in Fig. 1 where they are located in different regions of the $\Re e(k_z) - \Im m(k_z)$ plane, k_z being the normal component of the wave-vector in the refraction process between vacuum and the given medium. Primarily, we draw the readers' attention to the regions of the $\Re e(k_z) - \Im m(k_z)$ plane where the media with $\Re e(\epsilon) < 0$ and $\Re e(\mu) < 0$ lie. It is seen that they both have $\Re e(k_z) < 0$. Second, we also stress that refraction of waves is primarily a propagation effect that is interesting only when the waves can propagate long distances. While it has been theoretically shown that waves in some highly absorptive media can refract negatively across an interface, the propagation length of the wave inside the medium is usually so short to preclude even its experimental study in most cases.

During the past two years, there has been some controversy regarding the assignment of various physical media to these eight regions [22–26]. It has been wrongly suggested [23,24] that for light incident on a semi-infinite gain medium with $\Im m(\epsilon) < 0$, the presence of gain in the medium could imply a negative sign for the refractive index even if $\Re e(\epsilon) > 0$ and $\Re e(\mu) > 0$. It has also been mistakenly claimed [24] that evanescent waves that exponentially grow into bulk of the medium would exist at the interface of such a positive medium that has gain. While we will not get into a detailed analysis of this controversy here, we first note that for a finite medium such as a finite slab or a sphere, all the relevant physical quantities such as the transmission, reflection or scattering coefficients are invariant with the sign of the wave-vector or the index [26]. Hence the choice of the wave-vector in an infinite medium is primarily of academic curiosity. Second, the choice of the wave-vector that causes an exponential increase of the evanescent waves into the bulk of the medium would be contrary to the presence of surface plasmon waves at the interface between a metal and a gain medium that has been experimentally measured recently [27]. In any case, if the evanescent waves were to decay exponentially in absorptive media and amplify exponentially in amplifying media, the limit of zero dissipation or gain would become ill-defined. Hence the choice of a wave-vector that causes exponential amplification for evanescent waves in gain media is inconsistent. Finally, we should point out that the choice of the wave-vector in a gain medium has been investigated with careful experiments a long time ago [28]. The experimental results described therein clearly show that the sign for the square-root (or the wave-vector) in an amplifying positive dielectric medium is definitely positive. Hence we stress here that while there are two mathematically valid choices for the branch, the physical relevant branch for a medium can be chosen only by the imposition of physical boundary conditions. What

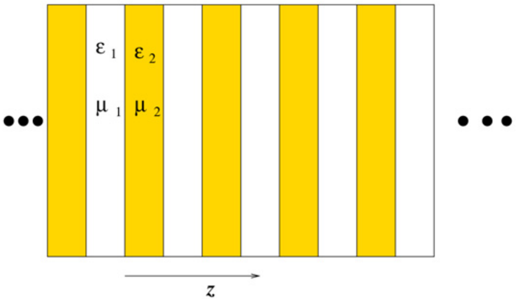

Fig. 2. Schematic picture of a periodically layered stack with alternating layers of materials with parameters (ϵ_1, μ_1) and (ϵ_2, μ_2) respectively. In the limit of thin layers and if one of the parameter set is negative, the stack behaves as an uniaxial indefinite medium.

boundary condition is physically correct can only be decided by experiments and there is unambiguous experimental evidence [28,27] that the choice of the signs for the wave-vector in various media and circumstances originally set out in Ref. [22] are the physically reasonable ones. We also note an attempt to obtain the limit of semi-infinite media by considering finite slabs with gain and taking the limit of infinite slab thickness [29] and remark that any such attempt would be futile for perfectly coherent, monochromatic waves as the steady-state solution is effectively obtained at infinite time where all the multiple reflections from both the interfaces, however far apart, are included in the solution.

3. Engineering negative effective medium parameters

While the negative dielectric permittivity demonstrated by a plasma and highly conducting metals at visible and ultra-violet frequencies has been known for over a century, negative magnetic permeability was relatively unknown except in some narrow frequency ranges in some magnetic materials at microwave frequencies. Natural materials with simultaneously negative dielectric and magnetic permeability were unknown and such effects became possible only with certain artificially structured materials, examples of which were first engineered during 1999–2001 [30,20,31].

In this section, we discuss how negative effective medium parameters can be obtained using two examples. In the first case, we present the homogenization analysis of a simple system of alternating layers of media with positive and negative effective parameters and show how it can lead to positive or negative effective medium anisotropic tensorial parameters. Such materials whose dielectric permittivity or magnetic permeability tensors have some positive components and some negative components are termed as indefinite media. These anisotropic materials have interesting properties: they can support the propagation of radiative modes that would be evanescent in usual positive media, and these modes travel in a preferred direction. The propagation of evanescent modes gives us hope that an image produced by light traveling through a slab of such a material might retain a sharp profile; also, because the preferred direction depends on the ratio of the components of the permittivity tensor, it can be controlled by varying the frequency of light used. In the second case, we present the split-ring resonator and thin wire media that demonstrate the essence of negative effective medium parameters: i.e., an anti-phased over-screened response at frequencies slightly greater than the resonance frequency of a forced oscillator with low levels of dissipation.

3.1. Layered media of alternating negative and positive layers: Smearing negativity around

Consider a periodically layered medium with alternating layers of positive and negative media. An easily realized canonical example would be a layered stack of thin layers of a dielectric medium such as silica and a good metal with negative dielectric permittivity such as silver or gold. For keeping the argument general and applicable to layers of structured metamaterials, let us assume that the alternating layers have thicknesses of d_1 and d_2 and have relative material parameters given by (ϵ_1, μ_1) and (ϵ_2, μ_2), respectively. This is schematically depicted in Fig. 2.

Now let us consider the limit of very thin layers, in which case the electric and magnetic fields in the layers will be reasonably uniform. They will, however, have to satisfy the conditions of continuity imposed by Maxwell's equations across the layer interfaces. Suppose the fields in the two layers are (E_1, D_1, B_1, H_1) and (E_2, D_2, B_2, H_2) respectively. First we account for the continuity of the tangential components across the interface and obtain

$$E_{1\tan} = E_{2\tan} = \langle E_{\tan} \rangle \tag{5}$$

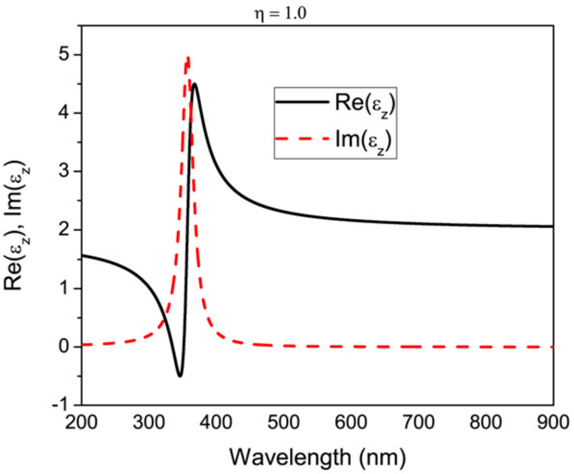

Fig. 3. The effective axial permittivity for a periodic layered stack of silver and silica when the volume fraction of silver is $\eta = 1$. The stack has the response of a resonant medium, which corresponds to the excitation of a plasmon mode across the structure.

$$H_{1\tan} = H_{2\tan} = \langle H_{\tan} \rangle \tag{6}$$

where $\langle\,\rangle$ indicates the average fields over a periodic cell. Now we can write for the volume averaged fields,

$$\langle D_{\tan} \rangle = f_1 D_{1\tan} + f_2 D_{2\tan} = \epsilon_0 \epsilon_\perp E_{1\tan} \tag{7}$$

$$\langle B_{\tan} \rangle = f_1 B_{1\tan} + f_2 B_{2\tan} = \mu_0 \mu_\perp H_{1\tan} \tag{8}$$

where $\perp$ indicates the tensorial component for fields applied perpendicular to the axis normal to the layers or tangential to the layers. Here $f_1 = d_1/(d_1 + d_2)$ and $f_2 = d_2/(d_1 + d_2)$, which gives the relative volume fractions of the two media. From the above, we obtain for the homogenized effective medium parameters,

$$\epsilon_\perp = f_1 \epsilon_1 + f_2 \epsilon_2 \tag{9}$$

$$\mu_\perp = f_1 \mu_1 + f_2 \mu_2 \tag{10}$$

Thus, the effective medium parameter components in the transverse direction are simple volume averages.

Similarly, considering the continuity of the normal components of the fields, we obtain

$$D_{1\text{norm}} = D_{2\text{norm}} = \langle D_{\text{norm}} \rangle \tag{11}$$

$$B_{1\text{norm}} = B_{2\text{norm}} = \langle B_{\text{norm}} \rangle \tag{12}$$

$$\langle E_{\text{norm}} \rangle = f_1 E_{1\text{norm}} + f_2 E_{2\text{norm}} \tag{13}$$

$$\langle H_{\text{norm}} \rangle = f_1 H_{1\text{norm}} + f_2 H_{2\text{norm}} \tag{14}$$

The above equations yield,

$$\epsilon_\parallel^{-1} = f_1 \epsilon_1^{-1} + f_2 \epsilon_2^{-1} \tag{15}$$

$$\mu_\parallel^{-1} = f_1 \mu_1^{-1} + f_2 \mu_2^{-1} \tag{16}$$

and we see that the reciprocal of the axial effective medium parameter is the volume average of the reciprocals of the layer medium parameters. There is, however, no mixing of the electric and magnetic responses. Such a mixing would require either a chirality or bianisotropy in one or both the layers of the periodic stack [32–34]. Also note that although the layer thickness does not figure explicitly in these expressions, the effective medium description is valid only in the limit of very thin layer thickness compared to the wavelength of radiation ($d_1, d_2 \ll \lambda$).

In fact, we have realized a very strange effective medium in the above discussion. The layered architecture of the stack results in extremely different responses to fields applied parallel and perpendicular to the axis normal to the layers. Depending on the relative values of ϵ_1 and ϵ_2, one could realize $\epsilon_\perp$ and $\epsilon_\parallel$ with opposite signs: i.e., the medium is an indefinite medium. In Fig. 3, we show the effective medium axial tensor components as a function of the wavelength for a layered stack consisting of alternating layers of silver and silica. The permittivity of silver is modeled by an empirical expression [1,35]

$$\epsilon_1(\lambda) = 5.7 + 0.4i - \left(\frac{9q}{2\pi c\hbar}\right)^2 \lambda^2 \tag{17}$$

where $q = 1.6 \times 10^{-19}$ C is the charge of an electron and $\hbar$ is the reduced Planck constant. This expression is valid for $\lambda \in (300, 900)$ nm. The dielectric permittivity of silica is typically modeled via a three resonance Sellmeier model [36]. We see that the mixture of positive and negative layers results in a resonant form for $\varepsilon_\|$ with a resonance at the wavelength where $\Re(\epsilon) \to 0$. This resonance frequency (or wavelength) is, of course, determined by the relative volume fractions. At wavelengths smaller than the resonance, the $\epsilon_\| < 0$, and at longer wavelengths $\epsilon_\|$ is positive. The other component $\epsilon_\perp$ is, however, negative at the longer wavelengths and we have a true indefinite dielectric medium.

The importance of indefinite media is that the dispersion for light becomes hyperbolic in these media [16]. Consider the dispersion equation in the above uniaxial medium for P-polarized light (when the magnetic field is normal to the axis, taken to be the z-axis)

$$\frac{k_x^2}{\epsilon_z} + \frac{k_z^2}{\epsilon_x} = \mu_y \frac{\omega^2}{c^2} \tag{18}$$

If $\epsilon_x/\epsilon_z < 0$, then we find that for very large k_x,

$$k_z = \pm\sqrt{\frac{-\epsilon_x}{\epsilon_z}} k_x \tag{19}$$

This is the quasi-static limit and the waves with large k_x almost have a specific direction of propagation in the indefinite uniaxial medium. Radiation with large transverse components of the wave-vector (transverse to the axis) propagates along a cone with a cone angle of

$$\theta = \tan^{-1}\sqrt{\frac{-\epsilon_z}{\epsilon_x}} \tag{20}$$

Such waves would be evanescent in an isotropic medium by comparison. This has potential implications for the design of imaging devices for the evanescent near-field modes as is discussed in Section 3.

Consider the reflection and transmission of a plane wave with a parallel wave-vector k_x, incident from vacuum onto the plane interface (x–y plane) between vacuum and a uniaxial effective medium with $\epsilon_x < 0$ and $\epsilon_z > 0$ (as it happens at wavelengths larger than the resonance wavelength in our above example) and a plane wave with a parallel wave-vector k_x to be incident from vacuum. Since k_x is fixed by the incident wave, we can obtain the wave-vector in the uniaxial medium from the dispersion relation as

$$k_z^2 = \mu_y \epsilon_x \frac{\omega^2}{c^2} - \frac{\epsilon_x}{\epsilon_z} k_x^2 \tag{21}$$

It is immediately seen that for $k_x < \sqrt{\epsilon_z \mu_y}\,\omega/c$, the light will become evanescent in the indefinite medium and for larger transverse wave-vectors become propagating in the indefinite medium. Thus, we will hence have total external reflection in such a scenario! The other case of $\epsilon_x > 0$ and $\epsilon_z < 0$, also results in an interesting case – the waves are always propagating in the indefinite medium for all k_x and hence we have no cut-off wave-vector in this situation, neither upper nor lower. This is easily seen from the iso-frequency plots of the refraction process shown schematically in Fig. 4. A variety of interesting refraction phenomena involving various kinds of indefinite media including the reversal of the Brewster and critical angles have been systematically studied in Ref. [37]. It must finally be emphasized that in all our discussions, we assume that the largest wave-vector considered must still be much smaller than the Bragg vector of the underlying periodic medium ($k_x \ll 2\pi/a$) in order to satisfy the conditions of homogenization and description by effective medium parameters.

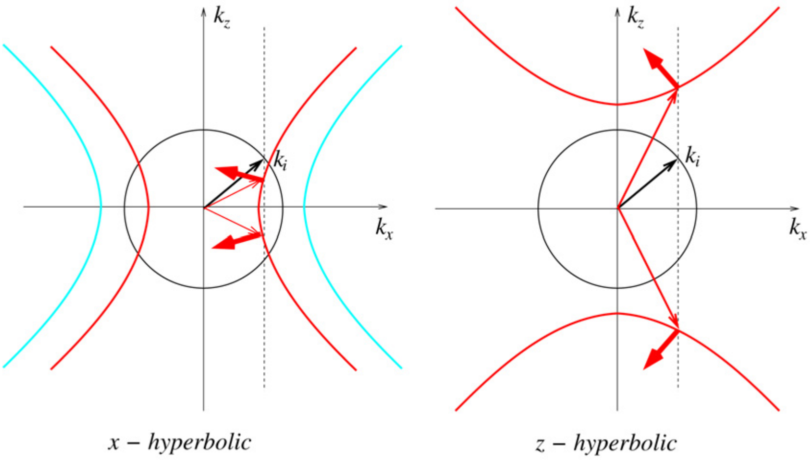

Fig. 4. Iso-frequency contour plots showing the negative refraction in an indefinite medium with hyperbolic dispersion. The circle in the center shows the iso-frequency contour for (isotropic) vacuum and the black arrow indicates the incident wave-vector. The red arrows indicate the wave-vector in the indefinite medium and the thick red arrows indicate the corresponding Poynting vectors. Left: for an x-hyperbolic medium with $\epsilon_x < 0$ and $\epsilon_z > 0$, the incident waves have a lower transverse wave-vector cut-off below which they do not couple to propagating modes in the hyperbolic medium. The blue hyperbolic dispersion curves indicate when no propagating modes in vacuum can couple to propagating modes in the medium. Right: the z-hyperbolic case of $\epsilon_x > 0$ and $\epsilon_z < 0$ when there is no cut-off wave-vector, either lower nor upper. Any propagating or evanescent wave incident from vacuum couples to propagating modes in the indefinite medium.

3.2. *Thin wire arrays: Doping the vacuum with metal*

It is well known that several metals behave as a plasma at optical and ultra-violet frequencies. Hence the dielectric permittivity given by

$$\epsilon(\omega) = 1 - \frac{\omega_p^2}{\omega(\omega + i\gamma)} \tag{22}$$

where ω_p is a plasma frequency and γ represents the dissipation rate, is negative for frequencies smaller than the plasma frequency ($\omega < \omega_p$). The plasma frequency for most good metals (with small γ) occurs at visible and ultra-violet frequencies, the most popular for plasmonic applications being silver and gold due to the low dissipation and the ease of handling them. However, due to the dissipation, this behavior cannot be readily extrapolated to lower frequencies, when $\gamma \sim \omega$, in the infra-red and microwave region of the spectrum.

It was shown by Pendry et al. [38,30] that a sparse array of thin wires would have a plasma like response at even microwave frequencies. Other groups including applied mathematicians have also subsequently derived this result [39–42]. The electric field of the radiation oriented along the wires would drive currents along the wires. The essential idea was that the sparseness of the wires yielded a reduced electron density (N_{eff}) and the thin wires gave rise to an enormous inductance to currents along the wire that made it appear as if the electrons moving in them had acquired very large effective masses (m_{eff}) that were thousands of times the bare electronic mass. The combined effect is to reduce the plasma frequency

$$\omega_p^2 = \frac{N_{\mathrm{eff}} e^2}{\epsilon_0 m_{\mathrm{eff}}} = \frac{2\pi c^2}{a^2 \ln(a/r)} \tag{23}$$

by several orders of magnitude. The plasma frequency only depends on the radius of the wires r and the spacing a as given by the above expression [38]. A three-dimensional wire array with wires extending along all the three wires will show a reasonably isotropic plasma-like response.

Using this simple recipe, thin wire metamaterials have been realized across the electromagnetic spectrum, down to microwave frequencies. Having finite wire strips instead of continuous wires results in a resonant response as the finite wire strips show the response of a bunch of electrical dipoles. A resonance arises due to the capacitive interaction of the adjacent wire segments in the line. The dielectric permittivity is now negative only within a finite band of frequencies above the resonant frequency. We refer the reader to Ref. [9] for more details on this topic. At optical frequencies

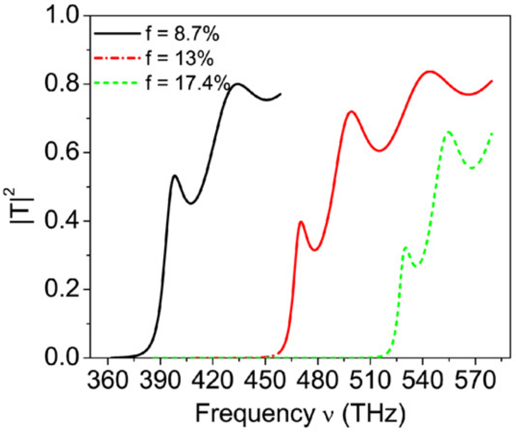

Fig. 5. Plot of the reflectivity and transmission through a periodic array of very long silver nanorods. The period of the array is 120 nm (subwavelength lengthscale) and the radiation is normally incident on the array with the electric field along the rods. A low frequency cut-off (ω_p) for the transmission that reduces with the rod size (filling fraction of the metal) is clearly seen demonstrating the behavior as a diluted metal.

and near infra-red frequencies, although the effect of the inductance is not predominant due to the penetration of the fields into the metallic wires, the volume fraction of the metal can be effectively used to tune the plasma frequency. For example, we show in Fig. 5, the reflection and transmission of light from an array of long silver wires calculated using the transfer matrix method. The polarization is such that the electric field of the light is along the wires which enables currents to be driven along the wires. There is a clear lower frequency cut-off which reduces with reducing wire thickness (or correspondingly the filling fraction, $f = \pi r^2/a^2$ where r is the radius of the wires and a is the unit cell size). Effectively, the system behaves as a diluted metal with a plasma frequency that depends on the square root of the filling volume fraction of the metal. This behavior is common to several 'holey' nanostructured metals. It has been shown [43] that arrays of subwavelength sized holes (with array spacing small compared to the wavelength) in a conducting metal film can support surface modes much in the manner of a plasma medium. This behavior turns out to be possible even if the film was made of a perfect conductor and only depends on the possibility that the geometry can support localized modes.

3.3. Negative magnetic permeability: An under-damped, overscreened resonance

While negative dielectric permittivity was known for plasmas, negative permeability was a rare occurrence in natural media that was only known to occur over very small bandwidths in resonant magnetic systems. Pendry et al. [20] introduced designs for structured media with $\mu < 0$, which paved the way for experimentalists to fabricate structures that gave rise eventually to negative refractive index materials. In fact, even today, most of the magnetic metamaterials structures have their origin in the designs of Ref. [20].

The simplest conceptual picture is best obtained for effectively two-dimensional systems with long cylinders with capacitive gaps running along them as shown in Fig. 6. If radiation is incident on this array of split-cylinders with the magnetic field oriented along the cylindrical axis as shown, the oscillating magnetic field induces currents to run around the conducting rings. These currents feel a finite inductive impedance (L) due to the finite size of the conducting loops while they feel a capacitive impedance (C) due to the capacitive gaps within the conducting loops. This gives rise to a resonant response of the system where the resonance is driven by the magnetic field of the radiation with a consequent resonant enhancement of the magnetic polarizability of the cylinder. If the array period is sufficiently small compared to the wavelength of the radiation, then it can be described by an effective medium magnetic permeability [20]

$$\mu_{\text{eff}} = 1 + \frac{f\omega^2}{\omega_m^2 - \omega^2 - i\gamma_m\omega} \tag{24}$$

where the resonance frequency $\omega_m^2 = 1/(LC)$ arises from the L-C resonance of the cylinders, f is the filling volume fraction of the split cylinders and γ_m is the dissipation that arises from the ohmic dissipation of the currents along

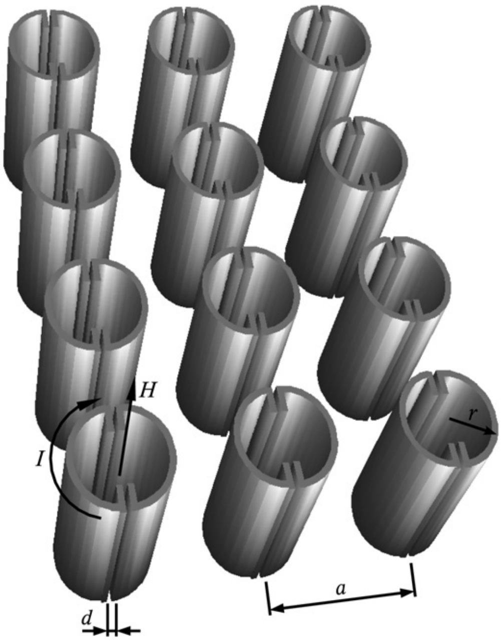

Fig. 6. Schematic picture of an array of cylinders with capacitive splits that respond resonantly to radiation with the magnetic field along the cylindrical axes. Circulating currents around the rings tend to shield the interior due to the inductance while the capacitance due to the gaps gives rise to a resonance.

the conducting loops. This magnetic permeability disperses violently near the resonance frequency. For a sufficiently small dissipation, the cylinders give rise to an overscreened response and the magnetic permeability becomes negative in a frequency band just above the resonance frequency ($\omega_m < \omega < \omega_m/\sqrt{1-f}$).

By proper choice of the size of the SRR and capacitive gaps, one could obtain a magnetic resonance at any desired frequency. Resonant magnetic metamaterials were quickly demonstrated at microwave frequencies [31], terahertz frequencies [44] and even mid infra-red frequencies [45]. However, scaling to higher and optical frequencies was not straightforward. It was pointed out in Ref. [46] that just making the SRR smaller could not reduce the inductance at large frequencies. With reducing size and increasing frequencies, the currents became essentially ballistic and the finite mass of the electrons contributes to an additional 'inertial' inductance that becomes comparable with the regular 'geometrical' inductance of the small SRR. It was shown in [47] that adding additional capacitive gaps could increase the resonant frequencies into the telecommunications frequencies by reducing the serial capacitance of the conducting loops. This predicted lack of linear scaling was later verified numerically [48] and SRR magnetic metamaterials have been experimentally demonstrated at NIR frequencies [49,50]. Meanwhile, numerical investigations of such SRR are undertaken to further understand its limitations and ways to overcome them [51,52].

However, alternative designs for high frequency (optical) magnetic materials have been demonstrated. Since the response of the metal consisting of the rings mostly has a plasma-like response, it is possible to remove large portions of the SRR and allow the displacement currents across these gaps to complete the circuit. Examples of such designs are the horse-shoe like SRR with one missing leg that provides the capacitance [53], metal rod pairs [54], and the fish-net structure [55]. The fish-net structure consists of a closely spaced double layer of thin films patterned as an anisotropic mesh and is designed for normal incidence of the waves. The magnetic field induces currents in opposite directions in appropriate legs of the double layer and is enhanced in the space in between the films. In all other designs such as the SRR, one needs to develop structures with a high aspect ratio that is difficult to manage at the nanometric scales that optical metamaterials require. Alú and Engheta [56] have proposed an alternate design for optical magnetic metamaterials that depends on plasmonic resonances of metallic nano-particles placed on subwavelength sized closed loops, which is yet to be demonstrated experimentally.

Completely homogenizable optical magnetic metamaterials have, however, proved elusive. In almost all cases, the underlying periodicity has almost been half the free-space wavelength. The plasma-like response of the metals (silver

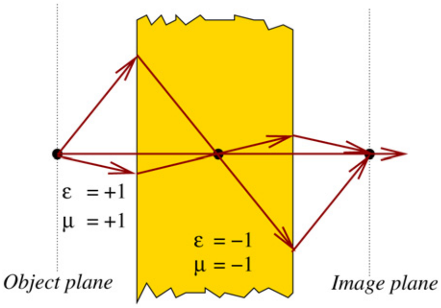

Fig. 7. Schematic picture showing the focussing of rays by a negative refractive index slab with $\epsilon = -1$ and $\mu = -1$, and surrounded by vacuum. A point source placed on one side will produce an image on the other side of the slab and also inside the slab. The entire object plane is mapped point-wise onto the image planes. The focussing action will be possible only if the distance from the source to the slab is smaller than the thickness of the slab.

or gold) and the practical limitations on size imposed by fabrication techniques make the size too large or otherwise the resonance is too weak. Description of the large sized (compared to wavelength) photonic systems by effective medium parameters is open to interpretation. A single set of anisotropic or even bianisotropic effective medium parameters cannot properly describe the optical metamaterials as these systems are highly spatially dispersive.

4. Perfect lenses and the principle of optical complementarity: Optical 'anti-matter'

In a manner similar to the White Queen who remembers events yet to come in Alice's Wonderland [57,58], light almost appears to propagate backwards in time within a negative index medium. The negative wave vector within a negative index medium implies, for instance, that the constant phase planes for a plane wave move backwards in time. The energy flow given by the Poynting vector **S** is, however, in the forward direction. This negative phase shift for light upon traverse through a negative index medium has an important consequence, that a flat slab of negative refractive index $n = -1$ can act as a lens (see Fig. 7).

Consider, for example, the transmission and reflection of light that is incident from vacuum on a slab of thickness, d, with $\epsilon = -1$ and $\mu = -1$. Let the parallel component of the wave-vector of the incident light be k_x, which is preserved in the refraction process and z be the imaging axis normal to the slab. The transmission and reflection coefficients of light of a slab (ϵ_2, μ_2) placed in a medium (ϵ_1, μ_1) can be calculated to be

$$T(k_x) = \frac{4Z_1 Z_2 \exp(ik_{z2}d)}{(Z_1 - Z_2)^2 - (Z_1 + Z_2)^2 \exp(2ik_{z2}d)} \tag{25}$$

$$R(k_x) = \frac{(Z_1^2 - Z_2^2)\exp(2ik_{z2}d)}{(Z_1 - Z_2)^2 - (Z_1 + Z_2)^2 \exp(2ik_{z2}d)} \tag{26}$$

where $Z_1 = k_{z1}/\epsilon_1$, $Z_2 = k_{z2}/\epsilon_2$, and k_{z1} and k_{z2} are the normal components of the wave-vectors in the respective media. In the limit of $\epsilon_2 = -\epsilon_1 = -1$ and $\mu_2 = -\mu_1 = -1$, the reflection and transmission coefficients become

$$T = \exp(-ik_{z2}d), \qquad R = 0 \tag{27}$$

for propagating waves. This is a consequence of the negative phase velocity in the medium 2. Hence, if one considers a point source located at a distance $d/2$ from the slab, any propagating wave that transmits through the slab arrives at a plane at a distance $d/2$ on the other side of the slab with exactly same phase as it started at the source. Further, the reflectivity of the slab is also zero due to perfect impedance matching. Thus the focussing action of the Veselago lens [2] (shown in Fig. 7) comes out in a straight forward manner for the propagating waves (rays).

Pendry [1] showed that the above focussing action holds not only for the propagating waves but also for the non-propagating evanescent near-field modes of a source. It is the evanescent near-field modes that have information about the variation of the electromagnetic fields on the object plane at lengthscales smaller than the wavelength of light. Consider the reflection and transmission coefficients for an incident wave $(\exp(-\kappa_z d))$. By analytic continuation of the result for the propagating waves $(k_z \rightarrow i\kappa_z)$, and we have

$$T = \exp(+\kappa_z d), \qquad R = 0 \tag{28}$$

Thus, the evanescent wave that usually decays exponentially with distance in free space increases exponentially with the thickness of the slab at exactly the same rate (κ_z). Hence the amplitude of the evanescent wave at the image plane at a distance $d/2$ from the slab becomes restored to exactly the same value as emitted by the source on the other side of the slab. The flat slab of $\epsilon = -1$ and $\mu = -1$ restores both the phase of the propagating waves and the amplitude of the evanescent waves, bringing all of them to a focus at the image plane. Hence it acts a perfect lens that is not limited by the conventional "diffraction" limit and can reproduce sub-wavelength sized features of the object in the image.

It was later on realized that the conditions for perfect lens action by a negative refraction index medium could be simplified. The lens could be built unsymmetrically with different media on either side of the negative medium slab [11], the negative index slab could be chopped up into thin layers [13], even other geometries such as cylindrical [59,8,60] and spherical geometries [4,61] were possible. These ideas can be garnered under a general theory of optical complementary media where in the negative index media behave in a complementary manner to ordinary media whereby they "undo" the effects of ordinary media on radiation. Combining this with a general method of co-ordinate mapping [62], one can map Maxwell's equations to other geometries and obtain perfect lenses in many geometries. For instance, using a mapping from a layered structure consisting of layers of complementary media together with a periodic set of line sources, it was observed in Refs. [4,63] that two negative 2D corners sharing the same corner combine to make an optical system within which light radiating from a line source is bent around a closed trajectory and is refocused back on to the line source.

4.1. A generalized lens theorem for electromagnetic complementary media

The original 'perfect lens' presupposed a uniform slab of isotropic material with dielectric permittivity $\epsilon = -1$ and magnetic permeability $\mu = -1$. However, focussing will occur under more general conditions [4,5]. Any system for which

$$\begin{aligned} &\epsilon_1 = +\epsilon(x_1, x_2), \qquad \mu_1 = +\mu(x_1, x_2), \qquad -d < x_3 < 0 \\ &\epsilon_2 = -\epsilon(x_1, x_2), \qquad \mu_2 = -\mu(x_1, x_2), \qquad 0 < x_3 < d \end{aligned} \tag{29}$$

will show identical focussing. Focussing will always occur irrespective of the medium in which the lens is embedded. This is true for any medium which is mirror antisymmetric about a plane. Thus, in general, a negatively refracting medium is complementary to an equal thickness of vacuum and optically 'cancels' its presence. The compensating action extends to both the evanescent as well as the propagating modes. Due to this, there is perfect transmission and the phase change of the transmitted wave is zero. In such systems, it is possible to excite surface plasmon modes at all spatial frequencies.

More generally, if we now consider a region of space described with general dielectric permittivity and magnetic permeability tensors given by

$$\underline{\underline{\varepsilon_1}} = \begin{pmatrix} \varepsilon_{11} & \varepsilon_{12} & \varepsilon_{13} \\ \varepsilon_{21} & \varepsilon_{22} & \varepsilon_{23} \\ \varepsilon_{31} & \varepsilon_{32} & \varepsilon_{33} \end{pmatrix}, \qquad \underline{\underline{\mu_1}} = \begin{pmatrix} \mu_{11} & \mu_{12} & \mu_{13} \\ \mu_{21} & \mu_{22} & \mu_{23} \\ \mu_{31} & \mu_{32} & \mu_{33} \end{pmatrix}, \qquad -d < x_3 < 0 \tag{30}$$

then the resulting complementary medium is given by

$$\underline{\underline{\varepsilon_2}} = \begin{pmatrix} -\varepsilon_{11} & -\varepsilon_{12} & +\varepsilon_{13} \\ -\varepsilon_{21} & -\varepsilon_{22} & +\varepsilon_{23} \\ +\varepsilon_{31} & +\varepsilon_{32} & -\varepsilon_{33} \end{pmatrix}, \qquad \underline{\underline{\mu_2}} = \begin{pmatrix} -\mu_{11} & -\mu_{12} & +\mu_{13} \\ -\mu_{21} & -\mu_{22} & +\mu_{23} \\ +\mu_{31} & +\mu_{32} & -\mu_{33} \end{pmatrix}, \qquad 0 < x_3 < d \tag{31}$$

which is the result first derived in [4] and retrieved using group theory (symmetries of Maxwell's equations) in Ref. [5]. The entries in $\underline{\underline{\varepsilon}}$ and $\underline{\underline{\mu}}$ can also be spatially varying along x and y. This covers the case of perfect corner reflectors of $2n$-fold skew-symmetry, and we are therefore ensured of the cancellation of the optical path. It is worth noting that the generalized lens theorem was also applied to infinite checkerboards of skew-symmetry in [5]. Let us now derive this theorem using the powerful tool of geometric transformations.

4.2. Perfect lenses via transformation optics

These matrices can be also computed using the viewpoint of transformation optics. For this, let us consider a map from a co-ordinate system $\{u_1, u_2, u_3\}$ to the co-ordinate system $\{x_1, x_2, x_3\}$ given by the transformation characterized by $x_1(u_1, u_2, u_3)$, $x_2(u_1, u_2, u_3)$ and $x_3(u_1, u_2, u_3)$. The transformation of the differentials is given by

$$\begin{cases} \mathrm{d}x_1 = \frac{\partial x_1}{\partial u_1}\,\mathrm{d}u_1 + \frac{\partial x_1}{\partial u_2}\,\mathrm{d}u_2 + \frac{\partial x_1}{\partial u_3}\,\mathrm{d}u_3 \\ \mathrm{d}x_2 = \frac{\partial x_2}{\partial u_1}\,\mathrm{d}u_1 + \frac{\partial x_2}{\partial u_2}\,\mathrm{d}u_2 + \frac{\partial x_2}{\partial u_3}\,\mathrm{d}u_3 \\ \mathrm{d}x_3 = \frac{\partial x_3}{\partial u_1}\,\mathrm{d}u_1 + \frac{\partial x_3}{\partial u_2}\,\mathrm{d}u_2 + \frac{\partial x_3}{\partial u_3}\,\mathrm{d}u_3 \end{cases} \tag{32}$$

This change of co-ordinates is characterized by the Jacobian of the transformation (32):

$$\mathbf{J_{xu}} = \frac{\partial(x_1, x_2, x_3)}{\partial(u_1, u_2, u_3)} = \begin{pmatrix} \frac{\partial x_1}{\partial u_1} & \frac{\partial x_1}{\partial u_2} & \frac{\partial x_1}{\partial u_3} \\ \frac{\partial x_2}{\partial u_1} & \frac{\partial x_2}{\partial u_2} & \frac{\partial x_2}{\partial u_3} \\ \frac{\partial x_3}{\partial u_1} & \frac{\partial x_3}{\partial u_2} & \frac{\partial x_3}{\partial u_3} \end{pmatrix}, \quad \text{with} \quad \begin{pmatrix} \mathrm{d}x_1 \\ \mathrm{d}x_2 \\ \mathrm{d}x_3 \end{pmatrix} = \mathbf{J_{xu}} \begin{pmatrix} \mathrm{d}u_1 \\ \mathrm{d}u_2 \\ \mathrm{d}u_3 \end{pmatrix} \tag{33}$$

This change of coordinates amounts to replacing the different materials (often homogeneous and isotropic, which corresponds to the case of scalar piecewise constant permittivities and permeabilities) by equivalent inhomogeneous anisotropic materials described by a transformation matrix $\mathbf{T}$ (metric tensor).

More precisely, Maxwell's equations retain their form under coordinate transformations, so that in the transformed coordinates Maxwell's operator writes as

$$\nabla \times \left(\underline{\underline{\mu}}'^{-1} \nabla \times \mathbf{E}\right) - \mu_0 \varepsilon_0 \omega^2 \underline{\underline{\varepsilon}}' \mathbf{E} = -i\omega\mu_0 \delta_{\mathbf{r}_s} \mathbf{p}, \quad \text{or } \nabla \times \left(\underline{\underline{\varepsilon}}'^{-1} \nabla \times \mathbf{H}\right) - \mu_0 \varepsilon_0 \omega^2 \underline{\underline{\mu}}' \mathbf{H} = \nabla \times \left(\underline{\underline{\varepsilon}}'^{-1} \mathbf{j}\right) \tag{34}$$

where $\mathbf{E}$ and $\mathbf{H}$ are the time-harmonic (complex vector valued) electric and magnetic fields oscillating at frequency ω (they are square integrable on every compact sub-manifold of $\mathbb{R}^3$), δ is the Dirac distribution supported by the source of polarization $\mathbf{p} \in \mathbb{C}^3$ located at $\mathbf{r}_s$, and $\mathbf{j}$ denotes a (distributed) current density. Last, but not least, $\varepsilon_0 \mu_0 = 1/c^2$ with c being the speed of light in vacuum and the transformed (anisotropic heterogeneous) media are characterized by [64–67]

$$\underline{\underline{\varepsilon}}' = \varepsilon \mathbf{T}^{-1}, \qquad \underline{\underline{\mu}}' = \mu \mathbf{T}^{-1}, \qquad \mathbf{T} = \frac{\mathbf{J}^T \mathbf{J}}{\det(\mathbf{J})} \tag{35}$$

Let us apply these mathematical tools to the slab perfect lens which is interesting in that it corresponds to a non-one-to-one coordinate transformation. This is clear, since it has triplets of planes on which the field distributions are identical: the object plane, the internal image plane and the external image plane. In the one-dimensional case, the corresponding coordinate transformation maps these three planes from a single plane in the reference space. The coordinate transformation is given by

$$\begin{cases} x'_1 = x_1 \\ x'_2 = x_2 \\ x'_3 = x_3 - d, \quad \text{if } x'_3 < -d/2, \quad \text{or } -x_3 \quad \text{if } -d/2 < x'_3 < d/2, \quad \text{or } x_3 + d, \quad \text{if } d/2 < x'_3 \end{cases} \tag{36}$$

where d is the thickness of the lens.

This leads to the identity for the transformation matrix $\mathbf{T}$ outside the lens, whereas inside the lens i.e. for $-d/2 < x'_3 < d/2$, $\partial x_3/\partial x'_3 = -1$ which flips the sign of T_{33}, so that the material properties differ from free space only in the $x_3 = x'_3$ direction, as expressed in (29), whereby the scalar permittivity $\varepsilon = \varepsilon_1$ and the transformed (scalar) permittivity $\varepsilon' = \varepsilon_2$, and similarly for the permeability.

However, in the case of anisotropic $\underline{\underline{\varepsilon}}$ and $\underline{\underline{\mu}}$, the transformed medium is now characterized by

$$\underline{\underline{\varepsilon}}' = \det(\mathbf{J})\left(\mathbf{J}^{-1} \underline{\underline{\varepsilon}} \mathbf{J}^{-T}\right) = (-1) \begin{pmatrix} 1 & 0 & 0 \\ 0 & 1 & 0 \\ 0 & 0 & -1 \end{pmatrix} \begin{pmatrix} \varepsilon_{11} & \varepsilon_{12} & \varepsilon_{13} \\ \varepsilon_{21} & \varepsilon_{22} & \varepsilon_{23} \\ \varepsilon_{31} & \varepsilon_{32} & \varepsilon_{33} \end{pmatrix} \begin{pmatrix} 1 & 0 & 0 \\ 0 & 1 & 0 \\ 0 & 0 & -1 \end{pmatrix}$$

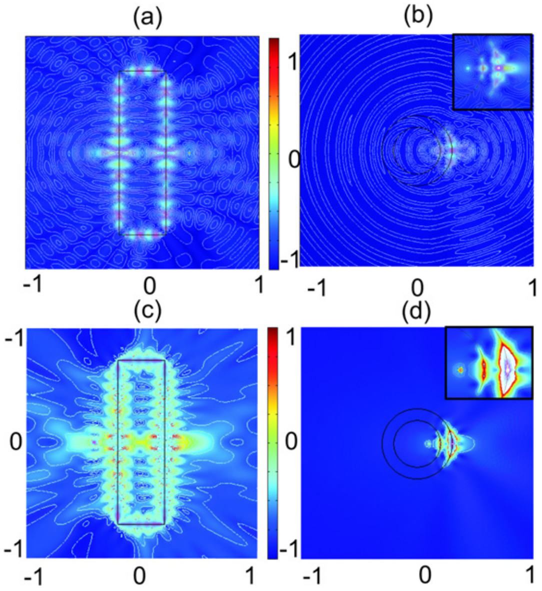

Fig. 8. Analysis of the electromagnetic field radiated by a harmonic line source in presence of a perfect lens with permittivity and permeability $\varepsilon = \mu = -1 + i * 0.004$. (a) Norm of electric field, slab lens; (b) Norm of electric field, cylindrical lens; (c) Norm of magnetic field, slab lens; (d) Norm of magnetic field, cylindrical lens. Insets in panels (b) and (d) are a magnification of the region surrounding the source and its image.

$$= \begin{pmatrix} -\varepsilon_{11} & -\varepsilon_{12} & +\varepsilon_{13} \\ -\varepsilon_{21} & -\varepsilon_{22} & +\varepsilon_{23} \\ +\varepsilon_{31} & +\varepsilon_{32} & -\varepsilon_{33} \end{pmatrix}$$

$$\underline{\underline{\mu}}' = \det(\mathbf{J})\big(\mathbf{J}^{-1}\underline{\underline{\mu}}\mathbf{J}^{-T}\big) = (-1)\begin{pmatrix} 1 & 0 & 0 \\ 0 & 1 & 0 \\ 0 & 0 & -1 \end{pmatrix}\begin{pmatrix} \mu_{11} & \mu_{12} & \mu_{13} \\ \mu_{21} & \mu_{22} & \mu_{23} \\ \mu_{31} & \mu_{32} & \mu_{33} \end{pmatrix}\begin{pmatrix} 1 & 0 & 0 \\ 0 & 1 & 0 \\ 0 & 0 & -1 \end{pmatrix}$$

$$= \begin{pmatrix} -\mu_{11} & -\mu_{12} & +\mu_{13} \\ -\mu_{21} & -\mu_{22} & +\mu_{23} \\ +\mu_{31} & +\mu_{32} & -\mu_{33} \end{pmatrix} \qquad (37)$$

which is in accordance with (31).

We note that there is no change in the impedance of the media, since the permittivity and permeability undergo the same geometric transformation: the perfect lens is impedance-matched with its surrounding medium (vacuum, say) so that no reflection will occur at its interfaces. In this way, one can design of plethora of generalized lenses [68–71], and this new field of physics has been named transformation optics.

The above derivation is straightforwardly extended to two-dimensional and three-dimensional perfect lenses, leading to (30), (31). The same arguments hold for cylindrical and spherical lenses, simply mapping Cartesian onto cylindrical-polar or spherical-polar coordinates. In the upper left panel of Fig. 8, we plot the norm of longitudinal electric field in the case of an electric line current source located at point $(x_1, x_2, x_3) = (x_1, 0, -0.3)$ in presence of a slab lens characterized by $\varepsilon(x_1, x_2, x_3) = \mu(x_1, x_2, x_3) = -1 + i * 0.004$ for $x_1 \in \mathbb{R}$, $-0.7 < x_2 < 0.7$, $-0.2 < x_3 < 0.2$. A 'ghost' image appears in the slab lens at $(x_1, 0, 0)$, whereas a 'perfect' image is visible at $(x_1, 0, 0.3)$. In the upper right panel of Fig. 8, we repeat this numerical experiment for a cylindrical perfect lens of inner radius $r_1 = 0.2$ and outer radius $r_2 = 0.3$ of permittivity $\varepsilon = -1 + i * 0.004$. A line source is located at point $(r_s, \theta_s) = (0.1, 0)$ with ghost image at point $(r_s', \theta_s') = (0.26, 0)$ and a perfect image at point $(r_s'', \theta_s'') = (0.36, 0)$.

4.3. *Triangular and square corner reflectors*

Among the large class of optical systems built by sticking together complementary media, we find the so-called corner lenses, or perfect corner reflectors. These represent very singular situations whereby the optical space can

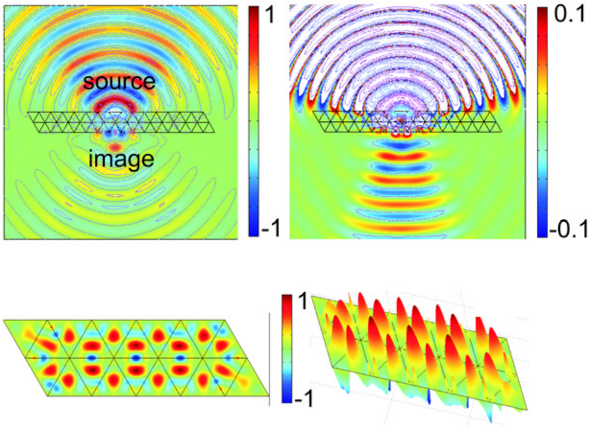

Fig. 9. Upper panel: Analysis of the electromagnetic field radiated inside the vacuum by a line source of wavelength $\lambda = 3a$, where a is the sidelength of each of the 60 regular triangular cells constituting the checkerboard lens. The source is located in the close neighborhood of this lens which alternates cells with relative permittivity and permeability $\varepsilon = \mu = 1$ and either $\varepsilon = \mu = -1 + i * 0.004$ (upper left) or $\varepsilon = \mu = -1 + i * 0.04$ (upper right). Lower panel: Analysis of the electromagnetic field radiated by the same line source line for a periodic checkerboard (the basic cell consists here of 20 regular triangles as in panel (c) of Fig. 15). In all four panels, we plot the real part of the longitudinal electric field.

be folded back onto itself in all three dimensions. In two dimensions, they are obtained by mapping a 1D photonic crystal onto a chessboard like structure via a change from Cartesian to polar coordinates. In three dimensions, we would rather start from a doubly periodic structure to get a three-dimensional chessboard like structure mapping Cartesian onto spherical coordinates.

The eigenfunctions of perfect corner reflectors can easily be written down in two dimensions. These are the periodic functions with periodicity of $[\pi, \pi]$

$$U(\theta, x_2, \ell) = \exp\bigl(\pm k_\theta |\theta|\bigr) \exp\bigl[\pm i(k_2 x_2 - \omega t) \pm k_\ell |\ell|\bigr] \tag{38}$$

in $\theta \in [-\pi/2, \pi/2]$. Here, $[k_\ell, k_\theta, k_2]$ are the eigenvalues satisfying $k_\ell^2 - k_\theta^2 - k_2^2 = \omega^2/c^2$. Thus we have one equation and three variables to be determined. Hence all modes with k_θ leading to the same k_2 and k_ℓ are degenerate at a given frequency and the density of modes diverges. This fact is illustrated in the lower panel of Fig. 9.

Understanding the perfect lens in terms of transformation designs is a great basis for understanding all the optical elements we discuss in this article. This is particularly true, since here we will consider not only slab elements, but also cylindrical and spherical lenses (transformation designed elements with non-parallel and non-planar surfaces prove useful for that). Perfect lenses are interesting in that they correspond to non-one-to-one coordinate transformations. This is especially obvious for the slab lens, since in that case the perfect lens has triplets of planes on which the field distributions are identical: the object plane, the internal image plane and the external image plane. The corresponding coordinate transformation (36) maps these three planes from a single plane in the reference space. But this is also true for a wider class of perfect lenses such as corner lenses made of a NRM sharing the perfect property of other negatively refracting lenses. This has been first shown in [4] using the technique of coordinate transformations. A pair of negatively refracting corners is capable of bending light in a loop and forming a series of images such that as $n \to -1$, light circulates within the loop forever. In the electrostatic limit, all the surface plasmon modes are degenerate at $\omega_p/\sqrt{2}$. At this frequency, the density of states diverges and $\epsilon = -1$, if we assume a simple Drude form for the plasma, $\epsilon = 1 - \omega_p^2/\omega(\omega + i\eta)$, where η is a small positive parameter.

In Fig. 10, we plot the norms of the electric and magnetic fields radiated by a harmonic line current source located inside an open resonator consisting of weakly absorptive square or triangular complementary regions. It is clear that the electromagnetic energy is mostly confined within the corner. In the limit when the resonator fills all the space and the absorption vanishes, all modes become infinitely degenerate, leading to a local density of states which diverges [63].

Also, it is worthwhile noting that the corner mode for the triangular perfect corner exhibits a C_{6v} symmetry (structure invariant through a rotation $2\pi/6$) while its counterpart for the square perfect corner is of C_{4v} symmetry. We preserve the symmetry of the structure for larger checkerboards but degeneracy means symmetry of modes is broken, which is a common feature in waveguide theory (see [72] for mode classes and degeneracies).

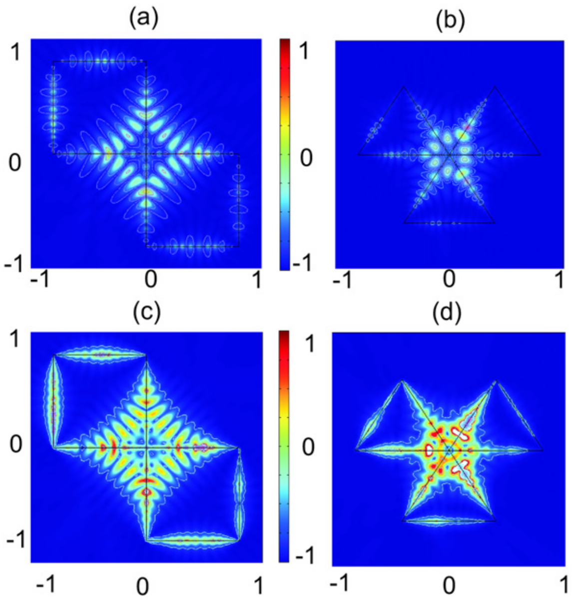

Fig. 10. Analysis of the electromagnetic field radiated by a line source located at $(x_1, x_2) = (0.2, 0.2)$ (square corners) and $(x_1, x_2) = (0, 0.2)$ (triangular corners). Upper panel: norm of the electric field; lower panel: norm of the magnetic field.

4.4. Superlenses with finite transverse extent

The original Pendry–Veselago lens assumed an infinite transverse extent for the slab of negative refractive index medium. When we consider structures such as the checkerboards, the structures are finite in more than one dimension and one natural question that comes up is regarding the effects of a finite transverse dimension on the image resolution. After all, in the case of the checkerboards one is transferring the images of such structures around with finite sized pieces of negative refractive index materials. For any practical implementation of superlenses where one would only have superlenses of finite transverse extent, this question assumes a technological significance. Even fundamentally, this question is of significance as aperture size of the lens in a conventional imaging system gives rise to diffraction and limits the smallest focus spot possible. For propagating waves, the finite aperture due to the finite transverse extent limits the waves with the largest transverse wave-vector that can be transported across the slab. However, the effects of the finite aperture on the evanescent waves cannot be that trivially understood. The finite transverse extent breaks the translational symmetry of the original problem and can generate waves with new transverse wave-vectors. In this section, we will analyze the effects of a finite transverse extent of Pendry's original flat lens.

This question has been analyzed earlier by [73,74] where it was found that in spite of a finite transverse width for the slab, much of the subwavelength image resolution was retained. Chen et al. [74] found that the image spectrum due to the finite slab was approximately given by the spectrum of the source itself multiplied by a convolution of the transmission coefficient and the Fourier transform of a window function that depended on the transverse extent of the slab. From numerical solutions of Maxwell's equations we find that the images with subwavelength resolution remain unaffected as long as the transverse width of the slab is not as small as the objects being imaged themselves. We show an example of the fields for imaging by a finite lens in Fig. 11 where the subwavelength image resolution can be clearly seen.

Here we analyze the effects of a finite transverse width using another approach. Obviously a full analytic solution for this problem will be highly non-trivial. We will model the effects of the finite transverse extent heuristically by assuming that the radiation incident outside this aperture is lost. To accomplish this, we assume that a slab of negative refractive index of infinite transverse extent is bounded by perfectly absorbing apertures as shown in Fig. 12. This is in fact equivalent to the well-known Kirchoff–Fresnel boundary conditions of the scalar diffraction theory [75]. In this approximate description, the effects of the finite transverse extent on the surface states that eventually determine the

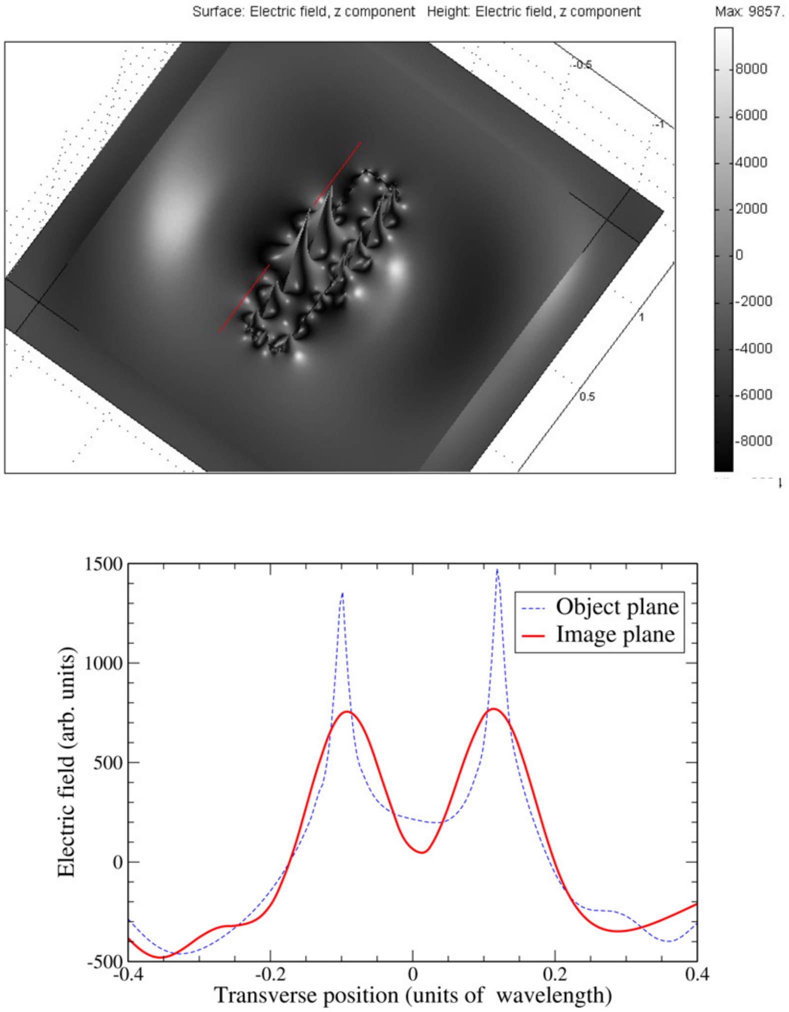

Fig. 11. Top: The electric fields of two line sources placed apart by 0.2λ imaged by a finite slab of width of λ calculated by a finite element method. Bottom panel: The electric fields at the object plane at a distance of 0.2λ from the slab and at a symmetrically placed image plane on the other side. The imaging and the subwavelength image resolution are clearly visible.

amplification of the evanescent waves and the subwavelength image resolution are not taken into account. Now the fields at the image plane can be obtained as

$$E(x,z_3) = F_x^{-1}\left\{e^{ik_z(z_3-z_2)}F_{k_x}\left[A_2(x)F_x^{-1}\left(T(k_x)F_{k_x}\left\{A_1(x)F_x^{-1}\left[e^{ik_z(z_1-z_0)}F_{k_x}E(x,z_0)\right]\right\}\right)\right]\right\} \tag{39}$$

where F_{k_x} and F_x^{-1} indicate the Fourier transform and the inverse Fourier transform respectively. $T(k_x)$ is the Fourier space transmission function of the slab of infinite transverse extent for an incident plane wave with wave-vector k_x and $k_x^2 + k_z^2 = \omega^2/c^2$ here. $A_1(x)$ and $A_2(x)$ are the aperture functions at the planes $z = z_1$ and $z = z_2$ respectively. We will assume that the aperture functions allow unit transmission within the aperture region (i.e., they are unity in a finite range of x) and zero transmission outside (they are zero outside). Essentially, here we propagate the fields to the edges of the slab where they are spatially modulated by the aperture functions. This is actually equivalent to the approximate solution of Chen et al. [74] where the image spectrum consists of a convolution of the transmission function and a window function. Here we have the direct spatial modulation or a multiplication of the spatial fields and the aperture functions. We now have provided a physical interpretation of the window function.

Let us examine the imaging of a pair of slits of widths 20 nm each and separated by a small sub-wavelength distance (100 nm) for different sizes of the transverse extent of the slab (modeled as the aperture size). We assume the radiation to have wavelength of 400 nm and the slab to have the material parameters of $\mu = -1$ and $\epsilon = -1 + i * 0.0001$. The

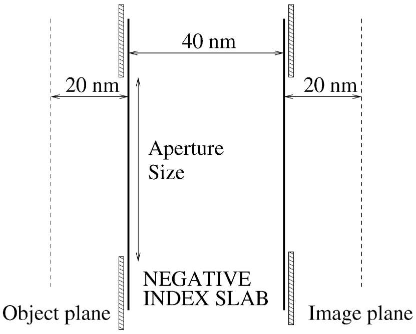

Fig. 12. Schematic picture showing the model for a superlens of finite transverse extent. The additional perfectly absorbing apertures in the front and back of the infinite slab imply that radiation incident outside this region is completely lost to the system.

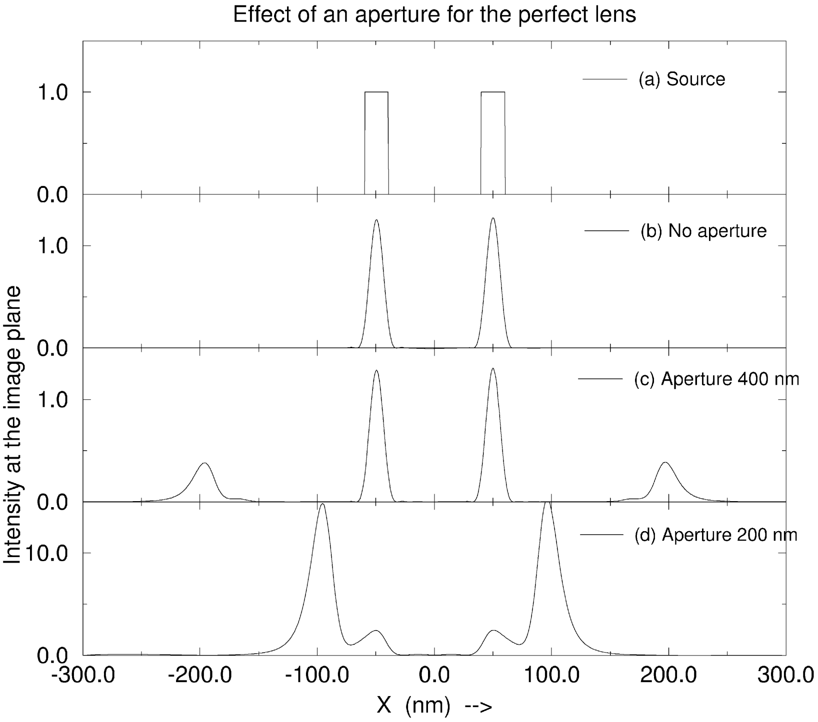

Fig. 13. The images of two slits of width 20 nm, placed apart by 100 nm (center-to-center) for different sizes of the aperture. The presence of the aperture becomes felt through an a shadow image of the edges which become more intense as the aperture size becomes similar to the lengthscales of the object being imaged itself.

small amount of dissipation is required for numerical purposes to prevent the mathematical divergences of the singular perfect lens without any dissipation. The finite dissipation, as is well known sets an upper cut-off for the wave-vectors which limits the image resolution [10]. The edges of the slits will not appear sharp in the image as a consequence. We show in Fig. 13 the images of the slits when imaged by apertures of various sizes. The finite extent of the aperture width creates its own image which can be seen when the aperture size is taken to be 400 nm ($\sim\lambda$) (c). However, even with such a small aperture, the resolution of the slits remains unchanged. We also note that the intense images of the aperture edges dominates the near-field images over that of the slits that are being imaged when the aperture size is about 200 nm (d). Thus, we conclude from this explicit demonstration that the finite transverse size of the slab will become important only when the aperture becomes almost of the same size as the objects that are being imaged. For a more absorptive slab, we have verified that the images of the aperture edges are of much lower intensity at the image plane along with a reduced resolution of the images. Of course, the full solution of the slab with finite transverse width

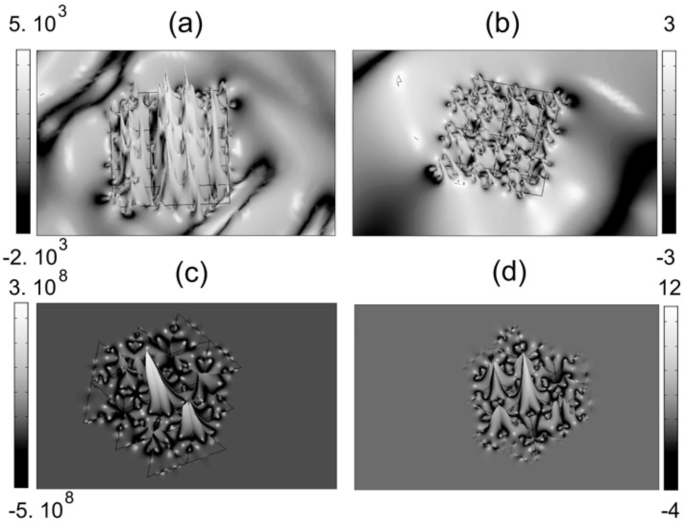

Fig. 14. Analysis of the longitudinal electric field radiated by a harmonic line source of wavelength $\lambda \sim 10a$ which is located inside a finite checkerboard consisting (a) of 36 square cells, (b) 26 equilateral triangles, of sidelength a which alternate relative permittivity and permeability $\varepsilon = \mu = 1$ and $\varepsilon = \mu = -1 + i * 0.04$; (c) Resonance of the square checkerboard at $\lambda \sim 10a + 0.1a$; Resonance of the triangular checkerboard at $\lambda \sim 10a + 0.00001a$. The strong leakage is noted in panels (b) and (c).

will be expected to also contain certain resonant features that arise due to the excitation of the plasmon modes of the finite slab that are not captured in this model as the slab is still assumed to be of infinite transverse extent.

4.5. Plasmonic resonances in infinite checkerboards

We next analyze infinite non-absorptive checkerboard structures, for which the imaginary part of the resonances should vanish. It has been shown in [5] that a source placed in one cell of a rectangular checkerboard produces an image in every other cell. This straightforwardly applies to triangular checkerboards as well, since they meet the property of mirror antisymmetry of the Generalized lens theorem, as can be observed in the lower panel of Fig. 9 where a source located in one NRM triangle of the basic cell produces an image in all other triangular complementary regions. These checkerboard structures retain their image transfer properties irrespective of whether they consist of homogeneous isotropic media or inhomogeneous anisotropic media, as long as they exhibit mirror antisymmetry and adjacent cells are complementary to each other.

All modes are degenerate at a given frequency $\omega_p/\sqrt{2}$ and the density of modes is infinite. These systems are extremely singular and contain a very large number of corners between positive and negative cells where the density of surface plasmon states diverges. Dissipation affects sub-wavelength imaging badly, and the divergence in the local density of states can only worsen the situation. It is due to this fact that the effect of dissipation on sub-wavelength resolution becomes an important issue, which we shall investigate in the sequel.

5. Resonant checkerboard configurations

5.1. The Ray picture does not always tell the truth

Let now consider finite checkerboards of NRM with square and equilateral triangular cells. From Fig. 14, it appears that the triangular checkerboard seem to do a better job at trapping light. For the triangular checkerboard shown in Fig. 15, the ray picture indicates the possibility of full reflection by a transverse generalized lens consisting of equilateral triangular cells. However, perfect transmission was found to occur in Fig. 9. This apparent contradiction of the full wave solutions with the ray analysis arises due to the localized fields at the corners which the rays cannot describe [76]. This extraordinary transmission occurs via the excitation of the surface plasmon modes of the system, as also transpires from Fig. 14. Nevertheless, the type of plasmonic guidance involved here via the interfaces between positive and negative index media differs substantially from the extraordinary transmission experimentally demonstrated

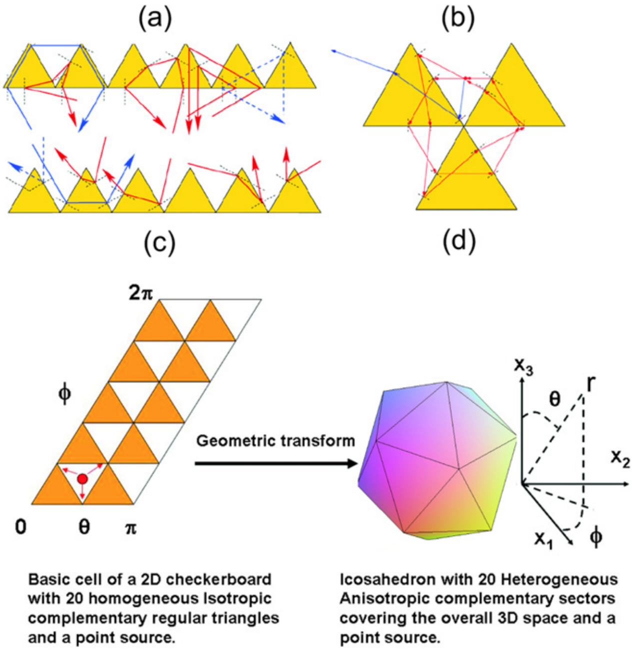

Fig. 15. (a) All rays incident on aligned triangular NRM are reflected; (b) Most rays emitted by a source located inside a triangular corner reflector circulate in closed trajectories (red trajectories) whereas others escape in free space (blue trajectories); (c) Basic periodic cell of 20 complementary regular triangles; (d) Icosahedral lens consisting of 20 complementary regions.

in [77], as we shall see in the sequel. As illustrated by the paradox of the ray picture showing no transmission and the complementary theorem showing perfect lensing (the optical path cancels), it is imperative to investigate numerically finite structures of NRM which are of the checkerboard type. This is why we also numerically checked the statement of the generalized lens theorem through finite element computations, as reported on Fig. 9, see also [78]. We numerically show in Fig. 9, the response of two small, slightly dissipative checkerboard systems consisting of cells alternating air and NRM (left: $\varepsilon = -1 + i * 0.04$ and $\mu = +1$; right: $\varepsilon = -1 + i * 0.004$ and $\mu = +1$), for a line source placed just above the checkerboard for the P-polarization. We note the flip of the sign for the field when it crosses the checkerboard, which we attribute to μ being non-negative. The checkerboard acts along the lines of the generalized lens theorem, even though it is of finite horizontal extent. Noteworthily, the dissipation in NRM on the left panel of Fig. 9 is quite large. Hence, the field enhancement is weakened on interfaces (which is why PML need not be taken far away), however, subwavelength imaging is displayed.

5.2. *Dissipative triangular and rectangular checkerboard systems*

We observed in our calculations that the eigenfunctions are large in magnitude, always located at the intersecting corners and very small in the bulk of the material. The working wavelength is typically larger than the cell's size, so that these corner modes are exponentially decaying away from the corners. We observe some surface plasmon excitations running along the interfaces separating complementary media. Since there is a large degeneracy of the modes, the leaky modes could be localized at any corner. From Fig. 14, we can see that the ratio of the real part to the imaginary part of the eigenfrequencies is larger for the triangular checkerboard, and accordingly the leakage reduces compared with square checkerboards. The rate of increase is faster for the case of triangular structure. From Fig. 14, we see that the amplitude of the cornermode increases with the symmetry of the system (fourfold for squares and sixfold for equilateral triangles).

Also, let us emphasize again that the corner mode for the triangular perfect corner exhibits a C_{6v} symmetry (structure invariant through a rotation $2\pi/6$) while its counterpart for the square perfect corner is of C_{4v} symmetry. We preserve the symmetry of the structure for larger checkerboards but degeneracy means symmetry of modes is broken, which is a common feature in waveguide theory (see [72] for mode classes and degeneracies). Interestingly, similar trapping effects occur in photonic crystal checkerboards [79]. However, the physics of negative refraction in photonic crystals does not involve plasmonic effects as in metamaterials [80], hence the LDOS is bound to remain finite even for infinite checkerboards (no control whatsoever of the evanescent field) [79].

6. Round trip in the flat land and its 3D counterpart

6.1. Mapping homogeneous isotropic checkerboards onto icosahedral 3D corner lenses

Let us consider a system of non-orthogonal coordinates (l,θ,Φ). These coordinates are along the directions of the lattice vectors attached to a triangular periodic checkerboard, whose basic cell is depicted in the left panel of Fig. 15. The associated material properties are expressed as

$$\begin{aligned}&\varepsilon(\theta,\Phi)=\mu(\theta,\Phi)=+1,\quad \forall(\theta,\Phi)\in \text{ Positive},\quad \text{and}\\ &\varepsilon(\theta,\Phi)=\mu(\theta,\Phi)=-1,\quad \forall(\theta,\Phi)\in \text{ Negative}\end{aligned}\tag{40}$$

where

$$\text{Positive}=(0,\pi/2)\times\left\{\bigcup_{j=0}^{N}\big[j\pi,(2j+1)\pi/2\big]\right\}\cup(\pi/2,\pi)\times\left\{\bigcup_{j=0}^{N}\big[(2j+1)\pi/2,(j+1)\pi\big]\right\}\tag{41}$$

and

$$\text{Negative}=(0,\pi/2)\times\left\{\bigcup_{j=0}^{N}\big[(2j+1)\pi/2,(j+1)\pi\big]\right\}\cup(\pi/2,\pi)\times\left\{\bigcup_{j=0}^{N}\big[j\pi,(2j+1)\pi/2\big]\right\}\tag{42}$$

This checkerboard is invariant along the l direction, periodic of period π in the θ direction and periodic of period 2π in the Φ direction. We want to analyze the electromagnetic field associated with a doubly periodic set of point sources within this two-phase positive–negative checkerboard (see Fig. 9) as shown in Fig. 15.

It is clear that a single source generates a point image inside every other block of the checkerboard. This can be easily shown by considering a singly periodic set of oblique slabs in either direction and using the generalized lens theorem [4,5] whereby the condition of complementarity is satisfied for the layers along the imaging direction with varying refractive index n in the direction transverse to the imaging direction.

From the knowledge of the field within the checkerboard containing the doubly periodic set of point sources (cf. Fig. 15, left panel), it is possible to find a solution of a 3D corner lens (cf. Fig. 15, right panel) mapping our system of generalized coordinates $(l,\ \theta,\ \Phi)$ onto Cartesian coordinates $(x_1,\ x_2,\ x_3)$ as follows:

$$l=\frac{l_0}{2}\ln\left(\frac{x_1^2+x_2^2+x_3^2}{r_0^2}\right),\qquad \theta=\arccos\left(\frac{x_3}{\sqrt{x_1^2+x_2^2+x_3^2}}\right)[\pi],\qquad \Phi=\arctan\left(\frac{x_2}{x_1}\right)[\pi]\tag{43}$$

where r_0 stands for the radial position of the point source on Fig. 15. Here, l denotes the radial (logarithmic) coordinate and θ and Φ denote the longitudinal and azimuthal coordinates.

Let us now defined three unit vectors $\mathbf{u}_1$, $\mathbf{u}_2$, $\mathbf{u}_3$ along the generalized l, θ, Φ axes. In the Cartesian frame (x_1,x_2,x_3) (see Fig. 15 left), we denote by $\tilde{\varepsilon}_{ij}$ (resp. $\tilde{\mu}_{ij}$) the nine non-zero components of the tensors $\tilde{\varepsilon}$ (resp. $\tilde{\mu}$) which are related to the *diagonal* tensors $\varepsilon(\theta,\Phi)$ (resp. $\mu(\theta,\Phi)$) as per [62]

$$\begin{aligned}&\tilde{\varepsilon}_{ij}=\varepsilon_i T_{ij}\big|\mathbf{u}_1\cdot(\mathbf{u}_2\times\mathbf{u}_3)\big|\frac{Q_1Q_2Q_3}{Q_iQ_j}\\ &\tilde{\mu}_{ij}=\mu_i T_{ij}\big|\mathbf{u}_1\cdot(\mathbf{u}_2\times\mathbf{u}_3)\big|\frac{Q_1Q_2Q_3}{Q_iQ_j},\quad i,j=1,2,3\end{aligned}\tag{44}$$

with $\mathbf{T}$ the metric tensor which is such that $T_{ij}^{-1}=\mathbf{u}_i\cdot\mathbf{u}_j$ and

$$Q_{ij}=\left(\frac{\partial l}{\partial x_i}\right)\left(\frac{\partial l}{\partial x_j}\right)+\left(\frac{\partial \theta}{\partial x_i}\right)\left(\frac{\partial \theta}{\partial x_j}\right)+\left(\frac{\partial \Phi}{\partial x_i}\right)\left(\frac{\partial \Phi}{\partial x_j}\right)\tag{45}$$

From (43) and (45) we deduce that

$$Q_{11} = \frac{1}{r}\sqrt{\cos^2 \Phi + \frac{\sin^2 \Phi}{\sin^2 \theta}}, \qquad Q_{22} = \frac{1}{r}\sqrt{\sin^2 \Phi + \frac{\cos^2 \Phi}{\sin^2 \theta}}, \qquad Q_{33} = \frac{1}{r} \tag{46}$$

Similar expressions hold for the other six Q_{ij}. Now, choosing

$$\begin{aligned} &\varepsilon_1 = \mu_1 = r\left(\frac{\sin^2\theta \cos^2\Phi + \sin^2\Phi}{\cos^2\theta \sin^2\Phi + \cos^2\Phi}\right) \\ &\varepsilon_2 = \mu_2 = \varepsilon_1^{-1} = \mu_1^{-1} \\ &\varepsilon_3 = \mu_3 = r\sin^2\theta \frac{\sqrt{\sin^2\theta \sin^2\Phi + \cos^2\Phi}}{\sqrt{\sin^2\theta\cos^2\Phi + \sin^2\Phi}} \end{aligned} \tag{47}$$

we get $\tilde{\varepsilon}_{ii}$, $\tilde{\mu}_{ii}$ to be identical to (40) and $\tilde{\varepsilon}_{ij} = \tilde{\mu}_{ij} = 0$, for $i \neq j$. This is the prescription for our new materials which will focus a source back onto itself in three dimensions. Note that this includes the near-field components as well.

The transformed electric and magnetic fields take the following forms:

$$\tilde{E}_i = Q_{ii}E_i, \qquad \tilde{H}_i = Q_{ii}H_i, \quad i \in \{1, 2, 3\} \tag{48}$$

where Q_{ii} is given by (46). We note that for rectangular checkerboards, the previous analysis simplifies since in that case $T_{ij}|\mathbf{u}_1 \cdot (\mathbf{u}_2 \times \mathbf{u}_3)| = \delta_{ij}$ [5].

We can build upon the previous algorithm and generate a checkerboard structure with as many complementary phases as we wish, provided that they respect mirror symmetries along the main diagonals, thereby generating multiphase 3D corner reflectors.

6.2. Spatially varying anisotropic checkerboards with sine-cosecant behavior

Consider a checkerboard with $\varepsilon_i(\theta, \Phi) = \pm\varepsilon_i \sin\theta$ or $\pm\varepsilon_i / \sin\theta$. It is clear that such a system satisfies the condition of complementarity and mirror symmetry, and therefore it should also image the sources as a checkerboard made of isotropic homogeneous materials. This is the sine-cosecant checkerboard that images the sources perfectly: using the property of mirror symmetry along θ about the positive–negative surfaces, we indeed obtain perfect mapping of a source onto an image. Hence, the icosahedral corner with the homogeneous materials with alternating signs for the refractive index will also form a cavity in a perfect sense. Thus, we have now generalized the result of [5] for a 3-D cubic corner to a 3-D icosahedral corner. There should be an infinite degeneracy of the associated surface states at frequency $\omega_p/\sqrt{2}$.

6.3. Homogeneous isotropic 3D checkerboards: Towards freezing light

According to the generalized lens theorem a periodic homogeneous isotropic checker icosahedral medium will also make a perfect lens if it satisfies the prerequisite mirror symmetry along all three imaging directions. A point source located within a cell will be imaged in every other cells. In this system of checker tetrahedra of complementary media, all surface plasma modes are degenerate at frequency $\omega_p/\sqrt{2}$ in the electrostatic limit. At this frequency, the density of states must be infinite. Also, this is a frequency at which the condition $\varepsilon = -1$ is met.

7. Conclusions

In this article, we reviewed and discussed some of the salient aspects of negative refractive index media and metamaterials, see also [80,58,9,81]. The origin of many of the strange effects on radiation in such media can be primarily traced to the negative phase vector. We gave examples of resonant metamaterials that can give rise to negative material parameters (ϵ, μ), and negative refractive index. The acute effects of anisotropy on radiation in metamaterials with some negative tensorial parameters was pointed out and can be of great consequence. Negative index materials can enable perfect lenses, in principle, due to their ability to support surface plasmon states, and this has been experimentally confirmed back in 2003 [82], and recently in the challenging case of volumetric super lenses [83]. After

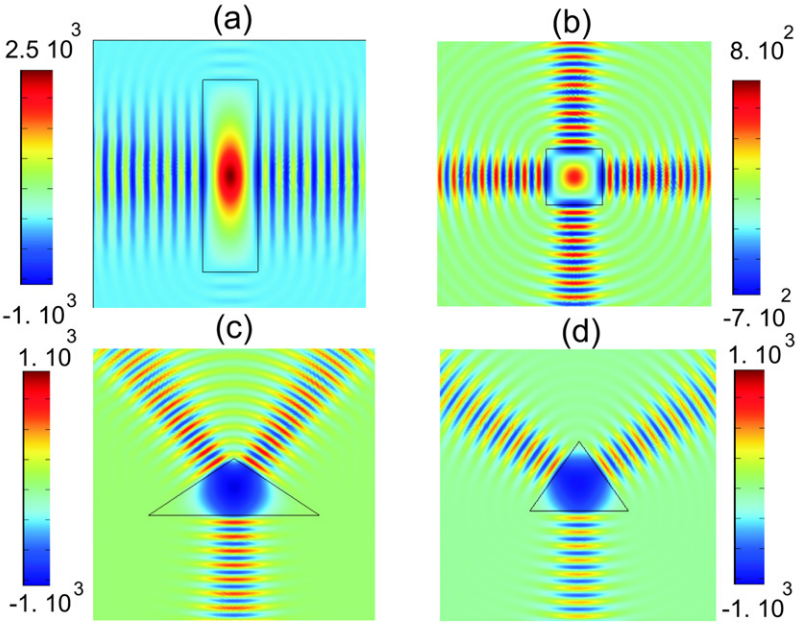

Fig. 16. Longitudinal electric field radiated by a line source of wavelength $\lambda = a$ located inside four metamaterials of typical sidelengths a filled an effective relative permittivity and permeability $\varepsilon = 0.01$ and $\mu = 1$. (a) Rectangle of width a and height $3.5a$; (b) Square of sidelength a; (c) Isosceles triangle of sidelengths a and $\sqrt{2}a$; (d) Equilateral triangle of sidelength a.

briefly reviewing the Pendry–Veselago lens (which displays neither astigmatism nor aberration [84]), we presented ideas of optical complementary media and generalized the perfect lens ideas to various geometries using a method of geometric transformations.

We have discussed possible extensions of perfect lenses to higher dimensional spaces and also checkerboard lenses paving the plane. The former have flat interfaces and can be shaped e.g. as boxes or tetrahedra. The latter are open resonators with counter-intuitive properties such as an infinite local density of states. The unifying viewpoint for all these optical systems is the concept of transformation optics whereby one can sculpt the refractive index ad libitum simply by mapping the optical space on what he likes. Although we focused here on the physics of negative refraction, it is worth mentioning that researchers have also investigated the case of a vanishing index of refraction. In that case, one essentially has a spatially constant field that is transmitted into the medium. Enoch et al. [85] have theorized an effective permittivity close to zero using some periodic array of metallic cylinders which enables to tune down the effective permittivity in a way similar to what was achieved by Pendry et al. [38] and Guida et al. [39] to obtain a low-frequency bulk plasmon. This has led to the realization of the first omni-directive antenna via ultra-refraction [85] and we give some examples of applications in Fig. 16.

While we focused our review on metamaterials which display unique effective properties in the homogenization regime, photonic crystals [86] offer an interesting alternative towards negative refraction in the Bragg regime, using anomalous dispersion curves located at the edges of stop bands (some of them naturally display a negative group velocity), as first theorized in [87] and then further explored in [88] (see also [81] for a comprehensive review of the state of the art in photonic crystals). Although sub-wavelength imaging remains elusive following this path, interest in this area has been recently fueled by some promising numerical simulations and experiments [89,90].

Finally, similar effects can be obtained for other types of waves, such as acoustic waves propagating in structured elastic materials [91–94,34] and even surface water waves interacting with periodic structures [95]. But other types of waves are also of interest, such as coupled pressure and shear elastic waves in structured solids, or flexural waves in thin structured plates. Enhanced resonances in opto-elastic metamaterials might even enable a better control of light via sound vibrations (via Brillouin scattering). Metamaterials with negative material parameters have created a novel route towards the control of radiation and hold much promise for future technologies including the recent exciting research in cloaking mechanisms. We are confident new discoveries are on their way.

Acknowledgements

The authors are thankful for funding to the Indo–French Centre for the Promotion of Advanced Research, New Delhi.

References

[1] J.B. Pendry, Negative refraction makes a perfect lens, Phys. Rev. Lett. 86 (2000) 3966.

[2] V.G. Veselago, The electrodynamics of substances with simultaneously negative value of ϵ and μ, Sov. Phys. Uspekhi 10 (1968) 509–514.

[3] R.C. McPhedran, N.A. Nicorovici, G.W. Milton, Optical and dielectric properties of partially resonant composites, Phys. Rev. B 49 (1994) 8479.

[4] J.B. Pendry, S.A. Ramakrishna, Focussing light using negative refraction, J. Phys.: Condens. Matter. 15 (2003) 6345–6364.

[5] S. Guenneau, A.C. Vutha, S.A. Ramakrishna, Negative refraction in 2D checkerboards by mirror anti-symmetry and 3D corner lenses, New J. Phys. 7 (2005) 164.

[6] S. Enoch, G. Tayeb, D. Maystre, Numerical evidence of ultrarefractive optics in photonic crystals, Opt. Commun. 161 (1999) 171–176.

[7] G.W. Milton, N.A. Nicorovici, On the cloaking effects associated with anomalous localized resonance, Proc. R. London A 462 (2006) 3027.

[8] J.B. Pendry, Perfect cylindrical lenses, Opt. Express 11 (7) (2003) 755–760.

[9] S.A. Ramakrishna, T.M. Grzegorczyk, Physics and Applications of Negative Refractive Index Materials, CRC Press, Boca Raton, 2009.

[10] D.R. Smith, D. Schurig, M. Rosenbluth, S. Schultz, S.A. Ramakrishna, J.B. Pendry, Limitations on subdiffraction imaging with a negative refractive index slab, Appl. Phys. Lett. 82 (10) (2003) 1506.

[11] S.A. Ramakrishna, J.B. Pendry, The asymmetric lossy near-perfect lens, J. Mod. Opt. 49 (10) (2002) 1747–1762.

[12] N. Fang, H. Lee, C. Sun, X. Zhang, Sub-diffraction-limited optical imaging with a silver superlens, Science 308 (2005) 534.

[13] S.A. Ramakrishna, J.B. Pendry, M.C.K. Wiltshire, W.J. Stewart, Imaging the near field, J. Mod. Opt. 50 (2003) 1419.

[14] Z. Jacob, L. Alekseyev, E. Narimanov, Optical hyperlens: far-field imaging beyond the diffraction limit, Opt. Express 14 (18) (2006) 8247–8256.

[15] A. Salandrino, N. Engheta, Far-field subdiffraction optical microscopy using metamaterial crystals: theory and simulations, Phys. Rev. B 74 (7) (2006) 751031.

[16] D.R. Smith, D. Schurig, Electromagnetic wave propagation in media with indefinite permittivity and permeability tensors, Phys. Rev. Lett. 90 (2003) 077405.

[17] Z. Liu, H. Lee, Y. Xiong, C. Sun, X. Zhang, Far-field optical hyperlens magnifying sub-diffraction-limited objects, Science 315 (5819) (2007) 1686.

[18] I. Smolyaninov, Y.-J. Hung, C. Davis, Magnifying superlens in the visible frequency range, Science 315 (5819) (2007) 1699.

[19] G. Shvets, S. Trendafilov, J. Pendry, A. Sarychev, Guiding, focusing, and sensing on the subwavelength scale using metallic wire arrays, Phys. Rev. Lett. 99 (2007) 053903.

[20] J.B. Pendry, A.J. Holden, D.J. Robbins, W.J. Stewart, Magnetism from conductors and enhanced nonlinear phenomena, IEEE Trans. Microwave Theory Tech. 47 (1999) 2075.

[21] A.B. Movchan, S. Guenneau, Split-ring resonators and localized modes, Phys. Rev. B 70 (2004) 125116.

[22] S.A. Ramakrishna, O.J.F. Martin, Resolving the wave vector in negative refractive index media, Opt. Lett. 30 (19) (2005) 2626.

[23] Y.F. Chen, P. Fischer, F.W. Wise, Negative refraction at optical frequencies in nonmagnetic two component molecular media, Phys. Rev. Lett. 95 (2005) 067402.

[24] J. Skaar, On resolving the refractive index and the wave vector, Opt. Lett. 31 (2006) 3372–3374.

[25] S.A. Ramakrishna, Comment on 'Negative refraction at optical frequencies in nonmagnetic two component molecular media', Phys. Rev. Lett. 98 (2007) 059701.

[26] A. Lakhtakia, J.B. Geddes III, T.G. Mackay, When does the choice of the refractive index of a linear, homogeneous, isotropic, active, dielectric medium matter? Opt. Express 15 (2007) 17709–17714.

[27] J. Seidel, F. Grafström, L. Eng, Stimulated emission of surface plasmons at the interface between a silver film and an optically pumped dye solution, Phys. Rev. Lett. 94 (2005) 177401.

[28] M.P. Silverman, And Yet It Moves, Cambridge Univ. Press, New York, NY, USA, 1993, pp. 151–163.

[29] V.U. Nazarov, Y.C. Chang, Resolving the wave vector and the refractive index from the coefficient of reflectance, Opt. Lett. 32 (2007) 2939–2941.

[30] J.B. Pendry, A.J. Holden, D.J. Robbins, W.J. Stewart, Low frequency plasmons in thin-wire structures, J. Phys.: Condens. Matter 10 (1998) 4785–4809.

[31] D.R. Smith, W.J. Padilla, V.C. Vier, S.C. Nemat-Nasser, S. Schultz, Composite medium with simultaneously negative permeability and permittivity, Phys. Rev. Lett. 84 (2000) 4184.

[32] S.A. Ramakrishna, A. Lakhtakia, Spectral shifts in the properties of a periodic multilayered stack due to isotropic chiral layers, J. Opt. A: Pure Appl. Opt. 11 (2009) 074001.

[33] S. Guenneau, F. Zolla, Homogenization of three-dimensional finite chiral photonic crystals, Physica B, doi:10.1016/j.physb.2006.12.021.

[34] G.W. Milton, J.R. Willis, On modifications of Newton's second law and linear continuum elastodynamics, Proc. R. Soc. London A 463 (2007) 855–880.

[35] F. Hao, P. Nordlander, Efficient dielectric function for FDTD simulation of the optical properties of silver and gold nanoparticles, Chem. Phys. Lett. 446 (2007) 115.

[36] J.A. Buck, Fundamentals of Optical Fibers, 2nd ed., John Wiley & Sons, Hoboken, NJ, USA, 2004, http://www.cvilaser.com. Also see for data sheets.

[37] T.M. Grzegorczyk, M. Nikku, X. Chen, B.-I. Wu, J.A. Kong, Refraction laws for anisotropic media and their applications to left-handed metamaterials, IEEE Trans. Microwave Theory Tech. 53 (2005) 1443–1450.

[38] J.B. Pendry, A.J. Holden, W.J. Stewart, I. Youngs, Extremely low frequency plasmons in metallic mesostructures, Phys. Rev. Lett. 76 (1996) 4773–4776.

[39] G. Guida, D. Maystre, G. Tayeb, P. Vincent, Electromagnetic modeling of three-dimensional photonic crystals, J. Elec. Waves Appl. 12 (1998) 1153–1179.

[40] D. Felbacq, G. Bouchitte, Homogenization of a set of parallel fibers, Waves Rand. Med. 7 (1997) 245.

[41] C.G. Poulton, S. Guenneau, A.B. Movchan, Non-commuting limits and effective properties for electromagnetism in conical incidence, Phys. Rev. B 69 (2004) 195112.

[42] K.D. Cherednichenko, V.P. Smyshlyaev, V.V. Zhikov, Non-local homogenized limits for composite media with highly anisotropic periodic fibers, Proc. R. Soc. Edinburgh A 136 (2006) 87.

[43] J.B. Pendry, L. Martin-Moreno, F.J. Garcia-Vidal, Mimicking surface plasmons with structured surfaces, Science 305 (2004) 847.

[44] T.J. Yen, W.J. Padilla, N. Fang, D.C. Vier, D.R. Smith, J.B. Pendry, D.N. Basov, X. Zhang, Terahertz magnetic response from artificial materials, Science 303 (2004) 1494.

[45] S. Linden, C. Enkrich, M. Wegener, J. Zhou, T. Koschny, C.M. Soukoulis, Magnetic response of metamaterials at 100 terahertz, Science 306 (2004) 1351–1353.

[46] S. O'Brien, J.B. Pendry, Magnetic activity at infrared frequencies in structured metallic photonic crystals, J. Phys.: Condens. Matter 14 (2002) 6383–6394.

[47] S. O'Brien, T. McPeake, S.A. Ramakrishna, J.B. Pendry, Near-infrared photonic band gaps and nonlinear effects in negative magnetic metamaterials, Phys. Rev. B 69 (2004) 241101.

[48] J. Zhou, Th. Kloschny, M. Kafesaki, E.N. Economou, J.B. Pendry, C.M. Soukoulis, Saturation of the mangetic response of split-ring resonators at optical frequencies, Phys. Rev. Lett. 95 (2005) 223902.

[49] G. Dolling, C. Enkrich, M. Wegener, C.M. Soukoulis, S. Linden, Low-loss negative-index metamaterial at telecommunication wavelengths, Opt. Lett. 31 (2006) 1800–1802.

[50] B. Kante, A. de Lustrac, J.M. Lourtioz, F. Gadot, Engineering resonances in infrared metamaterials, Opt. Express 16 (10) (2008) 6774–6784.

[51] R. Marques, F. Mesa, J. Martel, F. Medina, Comparative analysis of edge and broadside-coupled split ring resonators for metamaterial design – theory and experiments, IEEE Trans. Antennas Propag. 51 (10) (2003) 2572–2581, Part 1 (2004).

[52] M. Shamonin, E. Shamonina, V. Kalinin, L. Solymar, Resonant frequencies of a split-ring resonator: Analytical solutions and numerical simulations, Microwave Opt. Technol. Lett. 44 (2) (2005) 133–136.

[53] M.W. Klein, C. Enkrich, M. Wegener, C.M. Soukoulis, S. Linden, Single-slit split-ring resonators at optical frequencies: limits of size scaling, Opt. Lett. 31 (2006) 1259–1261.

[54] V.M. Shalaev, W. Cai, U.K. Chettiar, H. Yuan, A.K. Sarychev, V.P. Drachev, A.V. Kildishev, Negative index of refraction in optical metamaterials, Opt. Lett. 30 (2005) 3356–3358.

[55] S. Zhang, W. Fan, N.C. Panoiu, K.J. Malloy, R.M. Osgood, S.R.J. Brueck, Experimental demonstration of near-infrared negative-index metamaterials, Phys. Rev. Lett. 95 (2005) 137404.

[56] A. Alù, A. Salandrino, N. Engheta, Negative effective permeability and left-handed materials at optical frequencies, Opt. Express 14 (2006) 1557–1567.

[57] D. Maystre, S. Enoch, Perfect lenses made with left-handed materials: Alice's mirror? J. Opt. Soc. Am. A 21 (2004) 122–131.

[58] S. Guenneau, B. Gralak, Métamatériaux pour une lentille parfaite, La Recherche 401 (2006) 58–61.

[59] J.B. Pendry, S. Ramakrishna, Near-field lenses in two dimensions, J. Phys.: Condens. Matter 14 (36) (2002) 8463.

[60] G.W. Milton, N.A. Nicorovici, R.C. McPhedran, V.A. Podolskiy, A proof of superlensing in the quasistatic regime, and limitations of superlenses in this regime due to anomalous localized resonance, Proc. R. Soc. London A 461 (2005) 3999–4034.

[61] S.A. Ramakrishna, J.B. Pendry, Spherical perfect lens: Solutions of Maxwell's equations for spherical geometry, Phys. Rev. B 69 (2004) 115115.

[62] A.J. Ward, J.B. Pendry, Refraction and geometry in Maxwell's equations, J. Modern Opt. 43 (4) (1996) 773–793.

[63] S. Guenneau, B. Gralak, J.B. Pendry, Perfect corner reflector, Opt. Lett. 30 (2005) 1204.

[64] F. Zolla, G. Renversez, A. Nicolet, B. Kuhlmey, S. Guenneau, D. Felbacq, Foundations of Photonic Crystal Fibres, ICP Press, London, 2005.

[65] J.B. Pendry, D. Schurig, D.R. Smith, Controlling electromagnetic fields, Science 312 (2006) 1780.

[66] U. Leonhardt, T.G. Philbin, General relativity in electrical engineering, New J. Phys. 8 (2006) 247.

[67] A. Nicolet, F. Zolla, Y. Ould Agha, S. Guenneau, Geometrical transformations and equivalent materials in computational electromagnetism, Int. J. Comput. Math. Electrical Electronic Eng. COMPEL 27 (2008) 806–819.

[68] A.V. Kildishev, V.M. Shalaev, Engineering space for light via transformation optics, Opt. Lett. 33 (1) (2008) 43–45.

[69] M. Tsang, D. Psaltis, Magnifying perfect lens and superlens design by coordinate transformation, Phys. Rev. B 77 (3) (2008) 035122.

[70] D. Schurig, J.B. Pendry, D.R. Smith, Transformation-designed optical elements, Opt. Express 15 (22) (2007) 14772–14778.

[71] D. Schurig, J.B. Pendry, D.R. Smith, Calculation of material properties and ray tracing in transformation media, Opt. Express 14 (2006) 9794–9804.

[72] P.R. Mc Isaac, Symmetry-induced modal characteristics of uniform waveguides – II: Theory, IEEE Trans. Microwave Theory Tech. 23 (1975) 429.

[73] A.N. Lagarkov, V.N. Kissel, Near-perfect imaging in a focusing system based on a left-handed-material plate, Phys. Rev. Lett. 92 (2004) 077401.

[74] J.J. Chen, T.M. Grzegorczyk, B.-I. Wu, J.A. Kong, Imaging properties of finite-size left-handed material slabs, Phys. Rev. E 74 (2006) 046615.
[75] M. Born, E. Wolf, Principles of Optics, 7th ed., Cambridge University Press, Cambridge, UK, 1999.
[76] J.B. Pendry, Negative refraction, Contemp. Phys. 45 (2004) 191.
[77] T.W. Ebbesen, H.J. Lezec, T. Thio, P.A. Wolff, Extraordinary optical transmission through subwavelength hole arrays, Nature 391 (1998) 667–669.
[78] S. Chakrabarti, S.A. Ramakrishna, S. Guenneau, Finite checkerboards of dissipative negative refractive index, Opt. Express 14 (2006) 12950.
[79] S.A. Ramakrishna, S. Guenneau, S. Enoch, G. Tayeb, Light confinement through negative refraction in photonic crystal and metamaterial checkerboards, Phys. Rev. A 75 (2007) 063830.
[80] S.A. Ramakrishna, Physics of negative refraction, Rep. Prog. Phys. 68 (2005) 449.
[81] J.M. Lourtioz, H. Benisty, V. Berger, J.M. Gerard, D. Maystre, A. Tchelnokov, D. Pagnoux, Photonic Crystals: Towards Nanoscale Devices, Springer Verlag, Berlin, 2008.
[82] X. Parazzoli, C.G. Greegor, K. Li, B.E.C. Kontenbah, M.H. Tanielan, Experimental verification and simulation of negative index of refraction using Snell's law, Phys. Rev. Lett. 90 (2003) 107401.
[83] J. Zhu J, G.V. Eleftheriades, Experimental verification of overcoming the diffraction limit with a volumetric Veselago–Pendry transmission-line lens, Phys. Rev. Lett. 101 (1) (2008) 013902.
[84] D. Schurig, D. Smith, Negative index lens aberrations, Phys. Rev. E 70 (6) (2004) 65601.
[85] S. Enoch, G. Tayeb, P. Sabouroux, N. Guerin, P. Vincent, A metamaterial for directive emission, Phys. Rev. Lett. 89 (2002) 213902.
[86] E. Yablonovitch, Inhibited spontaneous emission in solid-state physics and electronics, Phys. Rev. Lett. 58 (1987) 2059.
[87] B. Gralak, S. Enoch, G. Tayeb, Anomalous refractive properties of photonic crystals, J. Opt. Soc. Am. A 17 (2000) 1012–1020.
[88] C. Luo, S.G. Johnson, J.D. Joannopoulos, J.B. Pendry, All-angle negative refraction without negative effective index, Phys. Rev. B 65 (2002) 201104.
[89] T. Decoopman, G. Tayeb, S. Enoch, D. Maystre, B. Gralak, Photonic crystal lens: From negative refraction and negative index to negative permittivity and permeability, Phys. Rev. Lett. 97 (2006) 073905.
[90] N. Fabre, L. Lalouat, B. Cluzel, X. Melenique, D. Lippens, F. de Fornel, O. Vanbesien, Optical near-field microscopy of light focusing through a photonic crystal flat lens, Phys. Rev. Lett. 101 (15) (2008) 073901.
[91] Z.Y. Liu, X.X. Zhang, Y.W. Mao, Y.Y. Zhu, Z.Y. Yang, C.T. Chan, P. Sheng, Locally resonant sonic materials, Science 289 (2000) 1734.
[92] J. Li, C.T. Chan, Double negative acoustic metamaterial, Phys. Rev. E 70 (2004) 055602.
[93] G.W. Milton, New metamaterials with macroscopic behavior outside that of continuum elastodynamics, New J. Phys. 9 (2007) 359.
[94] S. Guenneau, A.B. Movchan, G. Petursson, S.A. Ramakrishna, Acoustic meta-materials for sound focussing and confinement, New J. Phys. 9 (2007) 399.
[95] M. Farhat, S. Guenneau, S. Enoch, G. Tayeb, A.B. Movchan, N.V. Movchan, Analytical and numerical analysis of lensing effect for linear surface water waves through a square array of close to touching rigid square cylinders, Phys. Rev. E 77 (2008) 046308.